HHS Public Access

Author manuscript

Neuroimage. Author manuscript; available in PMC 2017 July 15.

Published in final edited form as:

Neuroimage. 2016 July 15; 135: 345–362. doi:10.1016/j.neuroimage.2016.02.039.

Q-space trajectory imaging for multidimensional diffusion MRI of the human brain

Carl-Fredrik Westin[1,2], **Hans Knutsson**[2], **Ofer Pasternak**[1], **Filip Szczepankiewicz**[3], **Evren Özarslan**[1,8], **Danielle van Westen**[4], **Cecilia Mattisson**[5], **Mats Bogren**[5], **Lauren O'Donnell**[1], **Marek Kubicki**[1], **Daniel Topgaard**[6], and **Markus Nilsson**[7]

[1]Brigham and Women's Hospital, Harvard Medical School, Boston, MA, USA

[2]Department of Biomedical Engineering, Linköping University, Linköping, Sweden

[3]Department of Medical Radiation Physics, Lund University, Lund, Sweden

[4]Department of Diagnostic Radiology, Lund University, Lund, Sweden

[5]Clinical Sciences, Psychiatry, Lund University, Lund, Sweden

[6]Division of Physical Chemistry, Department of Chemistry, Lund University, Lund, Sweden

[7]Lund University Bioimaging Center, Lund University, Lund, Sweden

[8]Department of Physics, Bogazici University, Istanbul, Turkey

Abstract

This work describes a new diffusion MR framework for imaging and modeling of microstructure that we call q-space trajectory imaging (QTI). The QTI framework consists of two parts: encoding and modeling. First we propose q-space trajectory encoding, which uses time-varying gradients to probe a trajectory in q-space, in contrast to traditional pulsed field gradient sequences that attempt to probe a point in q-space. Then we propose a microstructure model, the diffusion tensor distribution (DTD) model, which takes advantage of additional information provided by QTI to estimate a distributional model over diffusion tensors. We show that the QTI framework enables microstructure modeling that is not possible with the traditional pulsed gradient encoding as introduced by Stejskal and Tanner. In our analysis of QTI, we find that the well-known scalar b-value naturally extends to a tensor-valued entity, i.e., a diffusion measurement tensor, which we call the b-tensor. We show that b-tensors of rank 2 or 3 enable estimation of the mean and covariance of the DTD model in terms of a second order tensor (the diffusion tensor) and a fourth order tensor. The QTI framework has been designed to improve discrimination of the sizes, shapes, and orientations of diffusion microenvironments within tissue. We derive rotationally invariant scalar quantities describing intuitive microstructural features including size, shape, and orientation coherence measures. To demonstrate the feasibility of QTI on a clinical scanner, we performed a small pilot study comparing a group of five healthy controls with five patients with schizophrenia. The parameter maps derived from QTI were compared between the groups, and 9 out of the 14 parameters investigated showed differences between groups. The ability to measure and model the distribution of diffusion tensors, rather than a quantity that has already been averaged within a voxel, has the potential to provide a powerful paradigm for the study of complex tissue architecture.

Keywords

Diffusion MRI; q-space; DTI; microscopic anisotropy; microscopic fractional anisotropy μFA; QTI; q-space trajectory; SDE; DDE; TDE; diffusion tensor distribution

1 Introduction

Diffusion MRI (dMRI) encodes information on translational displacements of water on the micrometer scale [1]. Thus, the dMRI signal is an excellent probe for microstructural geometries in tissue such as the human brain. In dMRI, each millimeter-scale measurement contains an aggregate of information from a multitude of microscopic environments (microenvironments). The goal of our work is to disentangle the micrometer-scale information from these different microenvironments. In this paper we introduce a mathematical framework for advanced diffusion encoding, q-space trajectory imaging (QTI), and we propose a model for QTI data analysis, the diffusion tensor distribution (DTD). The QTI framework has been designed to improve discrimination of the sizes, shapes, and orientations of diffusion microenvironments within tissue. In the rest of this section, we describe related work for both aspects of our research: the diffusion encoding and the data modeling. We then give a summary of the main contributions of this paper.

The vast majority of dMRI applications today are based on the Stejskal-Tanner pulse sequence [2], which employs a single pair of pulsed magnetic field gradients for diffusion encoding. Here we refer to this sequence as the single diffusion encoding (SDE) experiment. The SDE technique is typically used in conventional diffusion tensor imaging (DTI) for quantification of measures such as the mean diffusivity (MD), the apparent diffusion coefficient (ADC) and the fractional anisotropy (FA) [3]. Techniques more advanced than DTI, such as high angular resolution diffusion imaging (HARDI) [4] and measurements of biophysical features such as axonal diameter [5, 6], are also typically based on the SDE experiment.

Measures derived from conventional SDE can identify subtle changes in tissue, but most measures provide limited insight into the nature of that change [7–9]. For example, many factors such as cell death, edema, inflammation, demyelination, increase in extracellular or intracellular water, and partial volume effects, may cause similar changes in FA [7, 10–13]. This limited specificity impedes our ability to relate measures from SDE to local anatomical changes and neuropathologies. Some of these limitations are specific to DTI and can be resolved by biophysical modeling and measurements with different diffusion times [5, 6]. Other limitations are inherent for SDE, for example its inability to disentangle variation in size and shape without prior information [14].

Alternative encoding methods have the potential to significantly improve tissue characterization beyond what is possible with SDE and DTI, increasing the sensitivity to microstructure. Such methods can, for example, provide information about distributions of cell shapes, sizes and membrane properties within a voxel [15, 16]. Many techniques have been proposed for advanced diffusion encoding. Some techniques employ multiple pairs of pulsed field gradients, where each pair performs a measurement in a certain direction, to

render the MR signal sensitive to higher order moments of the diffusion process. This category includes double diffusion encoding (DDE) sequences [17–19, 15, 20] and even triple diffusion encoding (TDE) sequences [21–24]. We are here using the recently proposed consensus nomenclature for diffusion methods extending beyond Stejskal and Tanner's design [25].

An alternative to multiple pulsed field gradients is to use time-varying gradients that are not pulsed, such as oscillating gradients [26], optimized gradient shapes [27], and rotating gradient fields or circularly polarized oscillating gradients [28, 29]. Our initial work used time-varying gradients to achieve an isotropic diffusion encoding [30], which can measure the trace of the diffusion tensor in a single shot. Recently, we have extended this work to investigate the use of more general time-varying gradients that specify a trajectory in q-space [31], which we call q-space trajectory encoding (QTE). By independently varying the experimental variables of the q-space trajectories, one can record a multidimensional dataset with information about the correlations between the observables in the different dimensions. Conceptually analogous multidimensional approaches revolutionized the field of nuclear magnetic resonance (NMR) spectroscopy [32] and were adapted to other techniques such as IR spectroscopy [33]. We therefore refer to these new encoding methods as multidimensional diffusion MRI, since they add additional dimensions to the acquisition that can be used to disentangle underlying features of the tissue.

Diffusion imaging methods are generally defined in terms of a diffusion encoding strategy plus a model of the signal. For example, for DTI, DKI (diffusional kurtosis imaging) and QTI we have the encoding and modeling relationships described in Table 1. In this work, we extend the diffusion tensor model with a fourth-order tensor that describes the covariance of diffusion tensors within a voxel, allowing us to define a novel yet intuitive diffusion tensor distribution model. Providing a complete overview of all proposed diffusion signal models is out of the scope of the current work. However, higher-order tensor models have previously been used to characterize non-Gaussian diffusion [34], in diffusional kurtosis imaging (DKI) [35] and in describing the variability of diffusion tensors estimated from DTI [36]. Diffusion tensor distributions have also been considered in the context of crossing fibers [37].

The QTI framework has been designed to improve discrimination of microenvironments within tissue. It is well known that the traditional FA measure confounds the dispersion of orientations with the shape of the microenvironments: in large white matter fiber bundles with one orientation, the FA reflects the geometry of the microenvironments, while in crossing fibers, the multiple fiber orientations will reduce the measured FA, confounding the connection to microstructure. The true microscopic anisotropy of the microenvironments has recently been modeled and estimated using DDE techniques [38, 39] and using isotropic diffusion encoding [14]. These microscopic FA (μFA) measurements are not confounded by orientation dispersion. In the current work, we introduce a distributional framework that naturally models orientation dispersion and microscopic anisotropy.

Within the QTI framework, we find that the familiar b-value naturally extends to a tensor-valued entity, a diffusion measurement tensor, which we call the b-tensor [40]. The b-tensor describes the second-order moment of the trajectory in q-space of the diffusion gradient

during an experiment. In current literature, the b-tensor is often referred to as the b-matrix. Although the b-matrix concept is well established and can be found in standard text books on diffusion NMR and MRI as a means to correct for crossterms from imaging gradients [41, 42, 1, 43], the characterization of the b-matrix for gradient diffusion encoding waveforms is a novel concept.

For the first time, we demonstrate estimation of a per-voxel diffusion tensor distribution directly from dMRI data. Using measurements obtained with trajectory encoding, we extend the diffusion tensor model with a fourth-order tensor that describes the covariance of diffusion tensors within a voxel, allowing us to define a novel yet intuitive diffusion tensor distribution model. We demonstrate that this estimation is possible with trajectory encoding but not with the traditional SDE. We use the concept of general b-tensor measurements, with multiple tensor shapes, to estimate the DTD. We compactly describe the DTD with a mean and covariance, and we show that the covariance information can be divided into two parts related to bulk and shear in materials science. We propose to separate the bulk and shear variances into measures that may be more intuitively meaningful, with the goal of separating size, shape, and orientation coherence. Finally, we demonstrate the clinical feasibility of QTI in a preliminary study of patients with schizophrenia and healthy controls.

2 Theory

QTI is a mathematical framework that combines trajectory encoding with a proposed data model, the diffusion tensor distribution. We describe how to use QTI to measure moments of the DTD and how to quantify these moments by invariant parameters that define microstructure information. We will explain how the new types of diffusion encodings can distinguish tissue architectures that are indistinguishable with conventional SDE-based dMRI. We motivate this here with a synthetic example: Figure 1 (top row) shows three diffusion tensor distributions that would all appear isotropic in an SDE experiment. Hence, they would be indistinguishable with conventional SDE-based dMRI sequences such as DTI, HARDI, DSI, and DKI. The proposed QTI framework can distinguish between these different cases to enable quantification of such differences in microstructure.

Throughout this paper, we will represent first-order tensors, i.e., vectors, by boldface italic letters (e.g. $\boldsymbol{n}$, size 3 × 1), second-order tensors by boldface capital letters (e.g. $\mathbf{D}$), and fourth-order tensors by blackboard bold capital letters (e.g. $\mathbb{C}$). Second-order tensors can be represented by 3×3 matrices, or if symmetric, in Voigt notation as vectors which we here express by corresponding lower-case letters (e.g. $\mathbf{d}$, size 6 × 1). Fourth-order tensors can be expressed using 3 × 3 × 3 × 3 elements. Symmetric fourth-order tensors can be represented more compactly by matrices (e.g. $\mathbb{C}$, size 6 × 6) or as vectors in Voigt notation (e.g. $\mathbb{c}$ size 21 × 1). The notation is explained in detail in the Appendix.

In this section we will first introduce the measurement tensor (the b-tensor) [40] and its connection to QTI. We will then discuss distributions over diffusion tensors and define the DTD model, its estimation using QTI, scalar invariants derived from DTD, and how to estimate these invariants.

2.1 Defining the b-tensor

In diffusion imaging, the measurement probe takes an average over the microenvironments within the tissue. By designing families of new probes, we are looking for statistical properties of the distribution over these microenvironments. We argue that by probing the collection of microenvironments with all shapes and orientations of measurement probes, we can recover information about the distribution over these microenvironments. For example, all three distributions in Figure 1 would appear isotropic in an SDE experiment, but can be distinguished with access to higher order moments such as variability in shape or size.

In conventional DTI, the dependence of the diffusion coefficient on the encoding direction $\boldsymbol{n}$ is modeled by a second-order tensor according to $D(\boldsymbol{n}) = \boldsymbol{n}^{\mathrm{T}}\langle\mathbf{D}\rangle\boldsymbol{n}$, where $|\boldsymbol{n}| = 1$. While DTI estimates a single second order tensor, it can be thought of as $\langle\mathbf{D}\rangle$, which is the mean of a distribution of tensors. This relation can also be expressed as an inner product between the diffusion tensor and a b-tensor **B** according to

$$bD(\boldsymbol{n}) = b\boldsymbol{n}^{\mathrm{T}}\langle\mathbf{D}\rangle\boldsymbol{n} = <b\boldsymbol{n}^{\otimes 2}, \mathbf{D}> = <\mathbf{B}, \mathbf{D}>. \quad (1)$$

where b is the b-value. Thus, in SDE, the b-tensor is defined by the outer product of the gradient direction, $\mathbf{B} = b\,\boldsymbol{n}^{\otimes 2} = b\,\boldsymbol{n}\boldsymbol{n}^{\mathrm{T}}$. The conventional b-value is given by $b =< \mathbf{B}, \mathbf{I} >$ where **I** is the second-order identity tensor. We may also express this as $b = \mathrm{Tr}(\mathbf{B})$, i.e., the trace of **B**. In the DTI literature, **B** is called the "b-matrix."

In the context of SDE-based acquisitions, the b-matrix is mainly used to correct for cross-terms with imaging gradients [44]. However, the b-matrix/tensor concept can be extended to analyze the diffusion encoding that results from waveforms other than SDE. In the most general form, we analyze the effect of an arbitrary time dependent gradient waveform $\boldsymbol{g}(t)$ in terms of a trajectory through q-space $\boldsymbol{q}(t)$ according to

$$\boldsymbol{q}(t) = \gamma\int_0^t \boldsymbol{g}(t')dt', \quad (2)$$

where γ is the gyromagnetic ratio. The b-tensor can now be generally defined as

$$\mathbf{B} = \int_0^\tau \boldsymbol{q}(t)^{\otimes 2}\,dt, \quad (3)$$

where τ is the echo time. To clarify, and as evidenced from equation 3, we note that the b-tensor is a measurement tensor, and as such it depends only on the gradient waveform and not on the underlying tissue geometry.

We emphasize that the trajectory of $\boldsymbol{q}(t)$ determines the *shape* of the b-tensor. To allow for an intuitive interpretation of the gradient trajectory and its relation to q-space and corresponding b-tensor, we illustrate a selection of b-tensors from SDE and DDE (Fig 2).

The shape of the b-tensor is quantified by its eigenvalues, and two b-tensors are of identical shapes if they share eigenvalues. In SDE, the b-tensors are of rank 1 (the rank of the b-tensor is given by the number of non-zero eigenvalues) and are shaped like a stick or a line, giving "linear" b-tensors. In DDE, when the two pulses are not parallel, the b-tensors have rank 2, and are shaped like a disc or a plane, producing a "planar" b-tensor. Gradient waveforms designed to yield isotropic diffusion encoding, for example TDE [23] or magic angle spinning of the q-vector (qMAS) [30], yield b-tensors of rank 3, shaped like spheres (Fig 3). The concept behind qMAS is to spin $\boldsymbol{q}(t)$ in order to narrow the distribution of diffusion coefficients to the the mean diffusivity of each domain, similar to the narrowing of chemical shift anisotropy obtained by mechanically spinning the sample in the magic-angle in solid-state NMR [45]. As we will show below, the rank of the b-tensor is important in the estimation of the DTD.

In general, any q-space trajectory starting and ending at the origin generates a b-tensor, and its shape will depend on the trajectory of the curve. Affine transformations may be used to modify the trajectory of the curve and the b-tensor [40]. To generate a b-tensor with a specific shape, one can start with a q-space trajectory $\boldsymbol{q}(t)$ that produces a b-tensor $\mathbf{B}$ (Eq. 3). Since Eq. 2 is linear, scaling $\boldsymbol{q}(t)$ with an affine transform $\mathbf{M}$ corresponds to scaling the gradient trajectory $\boldsymbol{g}_{\mathrm{M}}(t) = \mathbf{M}\,\boldsymbol{g}(t)$, and yields the new curve $\boldsymbol{q}_{\mathrm{M}}(t) = \mathbf{M}\boldsymbol{q}(t)$. This results in a new b-tensor

$$\mathbf{B}_{\mathrm{M}} = \int_0^\tau (\mathbf{M}\,\boldsymbol{q}(t))^{\otimes 2}\,dt = \mathbf{M}\left(\int_0^\tau \boldsymbol{q}_0^{\otimes 2}(t)\,dt\right)\mathbf{M}^{\mathrm{T}} = \mathbf{M}\,\mathbf{B}\,\mathbf{M}^{\mathrm{T}}. \quad (4)$$

The special case of transforming a normalized isotropic q-space trajectory with $\mathbf{B} = \mathbf{I}$ produces the simple relation $\mathbf{B}_{\mathrm{M}} = \mathbf{M}\mathbf{M}^{\mathrm{T}}$. Therefore, we can generate a family of trajectories with corresponding b-tensors by applying affine transforms to any existing gradient trajectory. Moreover, from a single trajectory that has a b-tensor of rank 3 (e.g., qMAS), we can generate new trajectories that span all possible b-tensors, i.e any set of three eigenvalues, at any orientation. Examples of affinely transformed trajectories and corresponding b-tensors can be found in figure 4.

We note that even if the trajectory $\boldsymbol{q}(t)$ corresponds to a $\mathbf{B}$ that is initially a rank 3 tensor yet not isotropic, the following transformation

$$\mathbf{M} = \mathbf{B}^{-1/2}, \quad (5)$$

will generate a new trajectory that yields a corresponding isotropic b-tensor, and can also transform $\boldsymbol{q}(t)$ to a trajectory that produces isotropic encoding. This is since $\mathbf{B}_{\mathrm{M}} = \mathbf{M}\,\mathbf{B}\,\mathbf{M}^{\mathrm{T}} = \mathbf{B}^{-1/2}\mathbf{B}(\mathbf{B}^{-1/2})^{\mathrm{T}} = \mathbf{I}$.

According to central concepts in image processing, efficient detection of signal is achieved by adapting the detection unit to the characteristics of the signal. Thus, we would like to

sample the signal with a variety of measuring b-tensors that span the entire family of shapes expected in the tissue microenvironments. For example, one natural option is a family of b-tensors that span the entire spectrum of shapes, from sticks through plates to spheres. When a linear and planar b-tensor are orthogonal, the linear tensor effectively encodes diffusion in a direction perpendicular to its planar counterpart, and visually, the linear b-tensor points along the normal of the plane of the planar b-tensor. Thus, there is a dual nature of a linear and planar b-tensor that share symmetry axes. In an anisotropic structure, a linear b-tensor oriented along the structure will yield higher signal attenuation, whereas the orthogonal planar tensor will yield lower signal attenuation.

An example of such encoding can be found in our recent work on TDE [24] where we use stick-sphere-plate b-tensors to measure stick-sphere-plane microscopic diffusion tensors. This proposed family of trajectories (Fig 4) was generated by applying affine transforms to an initially isotropic (i.e., spherical) qMAS encoding [14, 9] (Fig. 3, last row) as the initial input trajectory.

2.2 Defining a distribution over diffusion tensors

Consider a system composed of a collection of microenvironments, where in each individual microenvironment the diffusion is described by a diffusion tensor **D** (as in Fig. 1). We propose to compactly model these microenvironments within a voxel with a distribution over tensors. The tensor **D** is then a stochastic variable with expectation $\langle \mathbf{D} \rangle$, where $\langle \cdot \rangle$ represents averaging over the distribution in the voxel. The covariance of **D** is given by a fourth-order tensor $\mathbb{C}$ [36], that we define using the standard definition of covariance

$$\mathbb{C} = \langle \mathbf{D}^{\otimes 2} \rangle - \langle \mathbf{D} \rangle^{\otimes 2} \quad (6)$$

where $\mathbf{D}^{\otimes 2} = \mathbf{D} \otimes \mathbf{D}$ is the outer product of **D** with itself. For implementation, it is convenient to express the symmetric 3 × 3 tensor **D** in Voigt notation as a column vector **d** of size 6 × 1, containing the six distinct components of **D**, according to,

$$\mathbf{d} = \begin{pmatrix} d_{xx} & d_{yy} & d_{zz} & \sqrt{2}d_{yz} & \sqrt{2}d_{xz} & \sqrt{2}d_{xy} \end{pmatrix}^{\mathrm{T}}. \quad (7)$$

The $\sqrt{2}$ factors are necessary for **d** and **D** to have equal norms. The tensors $\langle \mathbf{D}^{\otimes 2} \rangle$ and $\langle \mathbf{D} \rangle^{\otimes 2}$ can now be defined by

$$\langle \mathbf{D}^{\otimes 2} \rangle = \langle \mathbf{d}\mathbf{d}^{\mathrm{T}} \rangle = \langle d_i d_j \rangle \quad (8)$$

where $i, j \in \{xx, yy, zz, yz, xz, xy\}$, and

$$\langle \mathbf{D} \rangle^{\otimes 2} = \langle \mathbf{d} \rangle \langle \mathbf{d} \rangle^{\mathrm{T}} = \langle d_i \rangle \langle d_j \rangle. \quad (9)$$

Hence, these tensors can be represented by 6 × 6 matrices. For the covariance $\mathbb{C}$, we reuse the same symbol for the 3 × 3 × 3 × 3 (Eq. 6) and the 6 × 6 versions of $\mathbb{C}$, which can now be expressed as

$$c_{ij} = \langle d_i d_j \rangle - \langle d_i \rangle \langle d_j \rangle, \quad (10)$$

or in full by

$$\mathbb{C} = \begin{pmatrix} c_{xx,xx} & c_{xx,yy} & c_{xx,zz} & \sqrt{2}c_{xx,yz} & \sqrt{2}c_{xx,xz} & \sqrt{2}c_{xx,xy} \\ c_{yy,xx} & c_{yy,yy} & c_{yy,zz} & \sqrt{2}c_{yy,yz} & \sqrt{2}c_{yy,xz} & \sqrt{2}c_{yy,xy} \\ c_{zz,xx} & c_{zz,yy} & c_{zz,zz} & \sqrt{2}c_{zz,yz} & \sqrt{2}c_{zz,xz} & \sqrt{2}c_{zz,xy} \\ \sqrt{2}c_{yz,xx} & \sqrt{2}c_{yz,yy} & \sqrt{2}c_{yz,zz} & 2c_{yz,yz} & 2c_{yz,xz} & 2c_{yz,xy} \\ \sqrt{2}c_{xz,xx} & \sqrt{2}c_{xz,yy} & \sqrt{2}c_{xz,zz} & 2c_{xz,yz} & 2c_{xz,xz} & 2c_{xz,xy} \\ \sqrt{2}c_{xy,xx} & \sqrt{2}c_{xy,yy} & \sqrt{2}c_{xy,zz} & 2c_{xy,yz} & 2c_{xy,xz} & 2c_{xy,xy} \end{pmatrix}, \quad (11)$$

where 21 out of the 36 elements are unique since $\mathbb{C}$ has both major symmetry ($c_{ab,cd} = c_{cd,ab}$) and minor symmetry ($c_{ab,cd} = c_{ba,cd}$). Note that this symmetry is different than for fully symmetric fourth-order tensors which have only 15 unique elements (c_{abcd} with fully permutable indices).

2.3 Diffusion modeling and estimation

The QTI framework describes the diffusion-encoded MR signal from a system composed of multiple microenvironments, each having Gaussian diffusion modeled by a diffusion tensor **D** and measured using a b-tensor **B**. The signal S (normalized by the non-diffusion weighted signal, S_0) can be expressed as

$$S(\mathbf{B}) = \langle \exp(-<\mathbf{B}, \mathbf{D}>) \rangle, \quad (12)$$

where $\langle \cdot\cdot \rangle$ averages the MR signal across all environments in a voxel. Assuming Gaussian diffusion in all microenvironments, it is sufficient to describe a QTI experiment by the b-tensor alone; other factors, such as the diffusion time or the duration of diffusion encoding, do not need to be explicitly accounted for. The abstraction of assuming Gaussian diffusion is useful and reasonably accurate as long as $1 > S(\mathbf{B}) > 0.1$ [46] and as long as any restricting geometries are small compared to the length scale of diffusion that takes place during the encoding waveform. This is also a central assumption, for example, in the NODDI model that assumes the apparent axonal diameter to be zero [47]

Investigating the cumulant expansion of S reveals a key relationship,

$$S(\mathbf{B}) \approx \exp\left(-<\mathbf{B}, \langle \mathbf{D} \rangle> + \tfrac{1}{2} <\mathbb{B}, \mathbb{C}>\right), \quad (13)$$

where $\mathbb{B}\,\mathbf{B}^{\otimes 2}$. This approximation enables us to relate $\langle \mathbf{D} \rangle$ and $\mathbb{C}$ from our model directly to the signal measurements. The derivation is presented in the Appendix, where we also show that expansion to the third order yields a 6th-order tensor that is related to the skewness of the distribution of diffusion tensors. The approximation in Eq. 13 is valid up to some b-value (trace of **B**) called the convergence radius, which depends on the distribution of the diffusion tensors. For simple distributions and for SDE, the convergence radius has been calculated analytically [48].

2.4 Scalar invariants derived from QTI

In this section, we introduce scalar invariants to describe properties of the distribution of microenvironments. We define these invariants using projections of $\langle \mathbf{D} \rangle$ and $\mathbb{C}$, and ratios of these projections. Figure 1 illustrates the tensors $\langle \mathbf{D} \rangle$ and $\mathbb{C}$ graphically for three distinct distributions of microenvironments, and example invariants.

Invariants from the mean of the tensor distribution—First, we note that existing DTI invariants can be expressed as inner products. For example, we can express the mean diffusivity (MD) as an inner product of the diffusion tensor and the isotropic tensor $\mathbf{E}_{\text{iso}}$ according to

$$\mathrm{MD}(\langle \mathbf{D} \rangle) = <\langle \mathbf{D} \rangle, \mathbf{E}_{\text{iso}}> = \left\langle \begin{pmatrix} d_{xx} & d_{xy} & d_{xz} \\ d_{yx} & d_{yy} & d_{yz} \\ d_{zx} & d_{zy} & d_{zz} \end{pmatrix}, \frac{1}{3} \begin{pmatrix} 1 & 0 & 0 \\ 0 & 1 & 0 \\ 0 & 0 & 1 \end{pmatrix} \right\rangle = \tfrac{1}{3}\left(d_{xx} + d_{yy} + d_{zz}\right) \quad (14)$$

where $\mathbf{E}_{\text{iso}}$ is defined by

$$\mathbf{E}_{\text{iso}} = \tfrac{1}{3}\mathbf{I} = \frac{1}{3} \begin{pmatrix} 1 & 0 & 0 \\ 0 & 1 & 0 \\ 0 & 0 & 1 \end{pmatrix}, \quad (15)$$

which is a scaled second-order identity tensor with unity Frobenius norm. In the next section we show that not only the mean, but also variances, can be expressed as inner products, and we use this to derive other scalar invariants of the distribution **D**.

Invariants from the covariance of the tensor distribution—From the 4th order covariance tensor, several scalar invariants can be derived. We start with discussing isotropic components of this tensor. We first define the isotropic 4th order tensor

$$\mathbb{E}_{\text{iso}}=\frac{1}{3}\begin{pmatrix}1&0&0&0&0&0\\0&1&0&0&0&0\\0&0&1&0&0&0\\0&0&0&1&0&0\\0&0&0&0&1&0\\0&0&0&0&0&1\end{pmatrix} \quad (16)$$

This isotropic fourth-order tensor can be divided into two distinct isotropic components, which in the field of mechanics are interpreted as bulk and shear modulus of the fourth-order stress tensor [49]. We define these tensors as

$$\mathbb{E}_{\text{bulk}}=\mathbf{E}_{\text{iso}}^{\otimes 2}=\frac{1}{9}\begin{pmatrix}1&1&1&0&0&0\\1&1&1&0&0&0\\1&1&1&0&0&0\\0&0&0&0&0&0\\0&0&0&0&0&0\\0&0&0&0&0&0\end{pmatrix} \quad (17)$$

and

$$\mathbb{E}_{\text{shear}}=\mathbb{E}_{\text{iso}}-\mathbf{E}_{\text{iso}}^{\otimes 2}=\frac{1}{9}\begin{pmatrix}2&-1&-1&0&0&0\\-1&2&-1&0&0&0\\-1&-1&2&0&0&0\\0&0&0&3&0&0\\0&0&0&0&3&0\\0&0&0&0&0&3\end{pmatrix}, \quad (18)$$

It is evident that the bulk and shear components are orthogonal, $<\mathbb{E}_{\text{bulk}}, \mathbb{E}_{\text{shear}}>= 0$.

These isotropic tensors can be used to derive scalar measures of variances from the fourth-order covariance tensor $\mathbb{C}$. For example, the variance in mean diffusivities V_{MD} between local microenvironments, is the bulk part of the variance,

$$V_{\text{bulk}}=<\mathbb{C},\mathbb{E}_{\text{bulk}}>=<\langle\mathbf{D}^{\otimes 2}\rangle,\mathbb{E}_{\text{bulk}}>-<\langle\mathbf{D}\rangle^{\otimes 2},\mathbb{E}_{\text{bulk}}>=V_{\text{MD}} \quad (19)$$

using the definition of $\mathbb{C}$ from (Eq. 6) and where

$$<\langle \mathbf{D}^{\otimes 2}\rangle, \mathbb{E}_{\text{bulk}}> = \langle \text{MD}^2\rangle \quad (20)$$

$$<\langle \mathbf{D}\rangle^{\otimes 2}, \mathbb{E}_{\text{bulk}}> = \langle \text{MD}\rangle^2 \quad (21)$$

Note that if $\mathbb{C}$ has been estimated, $\langle \mathbf{D}^{\otimes 2}\rangle$ can be obtained from $\mathbb{C}$ and $\langle \mathbf{D}\rangle$ (Eq. 6). The variance V_{MD} can be interpreted as the bulk or size variation of the diffusion tensors in the distribution and can in short be expressed as $V_{\text{MD}} = \langle \text{MD}^2\rangle - \langle \text{MD}\rangle^2$. Similarly, we obtain the shear variance V_{shear} by

$$V_{\text{shear}} = <\mathbb{C}, \mathbb{E}_{\text{shear}}> = <\langle \mathbf{D}^{\otimes 2}\rangle, \mathbb{E}_{\text{shear}}> - <\langle \mathbf{D}\rangle^{\otimes 2}, \mathbb{E}_{\text{shear}}> \quad (22)$$

This equation can be seen in terms of tensor-shape from eigenvalue variance. We can define the shape of a tensor **T** with eigenvalues λ_1, λ_2, and λ_3, according to

$$V_\lambda(\mathbf{T}) = \frac{1}{3}\sum_{i=1}^{3}\lambda_i^2 - \left(\frac{1}{3}\sum_{i=1}^{3}\lambda_i\right)^2. \quad (23)$$

With this definition the components of V_{shear} in Eq. 22 can be described by

$$<\langle \mathbf{D}^{\otimes 2}\rangle, \mathbb{E}_{\text{shear}}> = \langle V_\lambda(\mathbf{D})\rangle \quad (24)$$

$$<\langle \mathbf{D}\rangle^{\otimes 2}, \mathbb{E}_{\text{shear}}> = V_\lambda(\langle \mathbf{D}\rangle) \quad (25)$$

and the shear variance can be expressed as $V_{\text{shear}} = \langle V_\lambda(\mathbf{D})\rangle - V_\lambda(\langle \mathbf{D}\rangle)$. Further, the total isotropic variance is the sum of V_{MD} and V_{shear}

$$V_{\text{iso}} = <\mathbb{C}, \mathbb{E}_{\text{iso}}> = V_{\text{MD}} + V_{\text{shear}} \quad (26)$$

The shear variance V_{shear} is sensitive to both variations in orientation of the tensors, as well as the shape (microscopic anisotropy) of the tensors, in the distribution. It would yield a high value for a system containing randomly ordered anisotropic compartments (Fig. 1, left), and a low value for isotropic compartments (Fig. 1, middle). On the other hand, V_{MD} reflects variation of mean diffusivities and would yield a low value if all microscopic compartments are similar in this respect (Fig. 1, left), but a high value if they are not (Fig. 1, middle).

2.5 Normalized scalar invariants derived from QTI

We propose to separate the bulk and shear variances into measures that may be more intuitively meaningful, with the goal of separating size, shape, and orientation coherence. The measures we propose are normalized and range between 0 and 1. Normalizing the V_{MD} gives a natural size variation parameter, C_{MD}. Normalizing the shear variance is more challenging because it is affected by both the shape of the microenvironments and their orientation coherence (or dispersion). We derive a measure of shape, C_{μ}, related to μFA and a separate measure of microscopic orientation coherence, C_{c}, related to previously presented order parameters. Figure 5 summarizes the intuitive meaning of these measures.

Normalized size variance—This variance measure describes the normalized size variance of the tensors, where size is defined by the trace of the tensor, or equivalently by its mean diffusivity. A normalized size variance measure can be defined by normalizing V_{MD} (Eq. 19) to produce

$$C_{\mathrm{MD}} = \frac{<\mathbb{C},\, \mathbb{E}_{\mathrm{bulk}}>}{<\langle \mathbf{D}^{\otimes 2}\rangle,\, \mathbb{E}_{\mathrm{bulk}}>} = \frac{\sum \frac{1}{3}\mathrm{tr}(\mathbf{D}_k)^2 - \mathrm{tr}(\frac{1}{3}\sum \mathbf{D}_k)^2}{\sum \frac{1}{3}\mathrm{tr}(\mathbf{D}_k)^2} \quad (27)$$

where the subscript k indicates a sample from the distribution **D**, and the summation is over all samples. C_{MD} is 0 when all microenvironments have the same size, and increases with increased size variance.

Micro- and macroscopic anisotropy—We can also define a microenvironment shape measure using normalized variances. The obtained quantity C_{μ} is related to the microscopic anisotropy μFA of the tensors in the distribution

$$C_{\mu} = \frac{3}{2}\frac{<\langle \mathbf{D}^{\otimes 2}\rangle,\, \mathbb{E}_{\mathrm{shear}}>}{<\langle \mathbf{D}^{\otimes 2}\rangle,\, \mathbb{E}_{\mathrm{iso}}>} = \frac{3}{2}\frac{\sum_k (\frac{1}{3}\sum_{i=1}^{3}\lambda_{ki}^2 - (\frac{1}{3}\sum_{i=1}^{3}\lambda_{ki})^2)}{\frac{1}{3}\sum_k \sum_{i=1}^{3}\lambda_{ki}^2} = \mu\mathrm{FA}^2 \quad (28)$$

and thus

$$\mu\mathrm{FA} = \sqrt{C_{\mu}} \quad (29)$$

The factor $\frac{3}{2}$ makes the range of the measure [0,1]. Note that the averaging brackets $\langle\ \rangle$ in Eq. 28 are applied on the outer product of the tensors for each microdomain $\langle \mathbf{D}^{\otimes 2}\rangle$. By instead performing the averaging on the microdomain tensors and then taking the outer product $\langle \mathbf{D}\rangle^{\otimes 2}$, we arrive at an expression for the macroscopic anisotropy that corresponds to the familiar FA measure according to

$$C_{\mathrm{M}}=\frac{3}{2}\frac{<\langle\mathbf{D}\rangle^{\otimes 2},\,\mathbb{E}_{\mathrm{shear}}>}{<\langle\mathbf{D}\rangle^{\otimes 2},\,\mathbb{E}_{\mathrm{iso}}>}=\frac{3}{2}\frac{\frac{1}{3}\sum_{i=1}^{3}\lambda_i^2-\left(\frac{1}{3}\sum_{i=1}^{3}\lambda_i\right)^2}{\frac{1}{3}\sum_{i=1}^{3}\lambda_i^2}=\mathrm{FA}^2. \quad (30)$$

These two anisotropy measures C_{μ} and C_{M} become equal when all the tensors have the same shape and orientation. If there is dispersion of the orientations or variation in shape, then the two anisotropy measures are different. To illustrate the difference between these two anisotropy measures, consider a case when all tensors in a voxel have identical eigenvalues but are randomly oriented. In that case, C_{M} would be zero, but C_{μ} would assume the value that C_{M} would have had if all tensors were aligned. A corresponding analogy applies for FA and μFA [**?**], since they are simply the square roots of C_{M} and C_{μ}. Notice the similarity between Eqs. 28 and 30, where the only difference is whether the averaging across tensors takes place before or after the tensor outer product.

This way of calculating μFA is a direct method and does not involve any powder averaging as required by previous methods [14, 39]. Powder averaging requires that the sampling of the data is isotropically distributed on the sphere. For multiple diffusion encoding schemes, there is no general method for distributing the measurements isotropically. For double diffusion encoding, the few schemes that have been presented [39, 50, 51] have very specific numbers of measurements and cannot be varied when optimizing a clinical protocol.

Microscopic orientation coherence—The orientation coherence of microenvironments can by quantified by the orientational order parameter. The name “order parameter” is a well-established parameter for describing the order in liquid crystals. It is defined as $\mathrm{OP} = \langle 3\cos^2(\theta) - 1\rangle/2$, where θ is the angle between the domain and voxel scale symmetry axes. This original vector definition of the order parameter is based on the notion that the structures have the same size, and thus can be described by angles. This definition has recently been extended to (diffusion) tensors [14, 9]. Translated into our notation, these definitions of OP are

$$\mathrm{OP}^2=\frac{<\langle\mathbf{D}\rangle^{\otimes 2},\,\mathbb{E}_{\mathrm{shear}}><\langle\mathbf{D}^{\otimes 2}\rangle,\,\mathbb{E}_{\mathrm{bulk}}>}{<\langle\mathbf{D}^{\otimes 2}\rangle,\,\mathbb{E}_{\mathrm{shear}}><\langle\mathbf{D}\rangle^{\otimes 2},\,\mathbb{E}_{\mathrm{bulk}}>} \quad (31)$$

and

$$\mathrm{OP}^2=\frac{<\langle\mathbf{D}\rangle^{\otimes 2},\,\mathbb{E}_{\mathrm{shear}}>}{<\langle\mathbf{D}^{\otimes 2}\rangle,\,\mathbb{E}_{\mathrm{shear}}>} \quad (32)$$

OP provides a measure of orientation dispersion that has a simple geometric interpretation where OP = 0 indicates randomly oriented domain orientations and OP = 1 indicates perfectly coherent alignment.

We here define a new order parameter, C_c, the microscopic orientation coherence. C_c is related to prior definitions of OP, but it is designed to remove the effect of size distributions

$$C_c = \frac{<\langle \mathbf{D} \rangle^{\otimes 2}, \mathbb{E}_{\text{shear}}><\langle \mathbf{D}^{\otimes 2} \rangle, \mathbb{E}_{\text{iso}}>}{<\langle \mathbf{D}^{\otimes 2} \rangle, \mathbb{E}_{\text{shear}}><\langle \mathbf{D} \rangle^{\otimes 2}, \mathbb{E}_{\text{iso}}>} = \frac{C_{\text{M}}}{C_{\mu}}, \quad (33)$$

which we can recognize as the ratio of the micro- and macroscopic anisotropies. As an illustrative example, if all microenvironments are of the same shape and aligned, C_μ and C_M are equal, and thus C_c equals 1. If the microenvironments are randomly oriented, C_M becomes 0 and thus C_c equals 0. For very small C_μ this orientation coherence measures is not meaningful since the average orientation of the microenvironments is uncertain.

2.6 Connections to DKI

The QTI framework connects naturally to DKI [35], which is also based on the cumulant expansion of the signal (Eq. 13). The difference is that the fourth order tensor used in DKI, $\mathbb{W}$ is totally symmetric and thus has only 15 unique elements, which can be estimated from an SDE experiment. In contrast, $\mathbb{C}$ has major and minor symmetry with 21 unique elements, requiring acquisitions with b-tensors of rank 2 or 3. By comparing the DKI model from ref [35] with Eq. 13, we see that

$$<\tfrac{1}{3}\text{MD}^2\mathbb{W}, \boldsymbol{n}^{\otimes 4}> = <\mathbb{C}, \boldsymbol{n}^{\otimes 4}>. \quad (34)$$

However, $\frac{1}{3}\text{MD}^2\,\mathbb{W} \neq \mathbb{C}$, because $\mathbb{W}$has total symmetry whereas $\mathbb{C}$ has not. This has consequences for the metrics that can be derived. It can be shown that

$$2<\mathbb{W}, \mathbb{E}_{\text{bulk}}> = <\mathbb{W}, \mathbb{E}_{\text{shear}}>. \quad (35)$$

This means that DKI entangles the bulk and shear contributions to the tensor variance. To more explicitly see this, we will derive the totally symmetric isotropic tensor (15 unique elements), and express it by a bulk and a shear component. Consider the mean kurtosis, here defined as the average of $\mathbb{W}$across the sphere as [52]

$$\text{MK} = \frac{1}{4\pi}\int_{|\boldsymbol{n}|=1} <\mathbb{W}, \boldsymbol{n}^{\otimes 4}> dS \quad (36)$$

which in our notation is written as

$$\mathrm{MK}=<\mathbb{W},\mathbb{E}_{\mathrm{tsym}}>=3\frac{<\mathbb{C},\mathbb{E}_{\mathrm{tsym}}>}{<\langle\mathbf{D}\rangle^{\otimes 2},\mathbb{E}_{\mathrm{bulk}}>} \quad (37)$$

where $\mathbb{E}_{\mathrm{tsym}}$ is an isotropic tensor that has total symmetry (15 independent components), defined as

$$\mathbb{E}_{\mathrm{tsym}}=\frac{1}{4\pi}\int_{|\boldsymbol{n}|=1}\mathbf{n}^{\otimes 4}\,dS=\frac{1}{15}\begin{pmatrix}3&1&1&0&0&0\\1&3&1&0&0&0\\1&1&3&0&0&0\\0&0&0&2&0&0\\0&0&0&0&2&0\\0&0&0&0&0&2\end{pmatrix}=\mathbb{E}_{\mathrm{bulk}}+\tfrac{2}{5}\mathbb{E}_{\mathrm{shear}} \quad (38)$$

From Equation 38, and the fact that the bulk and shear components are orthogonal, we can see that the ratio of the inner products with the shear and bulk tensor

$$\frac{<\mathbb{E}_{\mathrm{tsym}},\mathbb{E}_{\mathrm{shear}}>}{<\mathbb{E}_{\mathrm{tsym}},\mathbb{E}_{\mathrm{bulk}}>}=\frac{2<\mathbb{E}_{\mathrm{shear}},\mathbb{E}_{\mathrm{shear}}>}{5<\mathbb{E}_{\mathrm{bulk}},\mathbb{E}_{\mathrm{bulk}}>}=\frac{2}{5}\frac{45}{81}\frac{81}{9}=2, \quad (39)$$

which is the factor 2 in equation 35.

Disentangling bulk and shear kurtosis by QTI—From equation 38 we see that $\mathbb{E}_{\mathrm{tsym}}$ is the sum of a bulk and shear part, and thus DKI's mean kurtosis is also the sum of two kurtosis components

$$\mathrm{MK}=K_{\mathrm{bulk}}+K_{\mathrm{shear}}. \quad (40)$$

With access to the full 4th order tensor $\mathbb{C}$, QTI allows the estimations of the two separate kurtosis contributions. We denote these two novel measures the bulk kurtosis,

$$K_{\mathrm{bulk}}=3\frac{<\mathbb{C},\mathbb{E}_{\mathrm{bulk}}>}{<\langle\mathbf{D}\rangle^{\otimes 2},\mathbb{E}_{\mathrm{bulk}}>}, \quad (41)$$

and the shear kurtosis,

$$K_{\mathrm{shear}}=\frac{6}{5}\frac{<\mathbb{C},\mathbb{E}_{\mathrm{shear}}>}{<\langle\mathbf{D}\rangle^{\otimes 2},\mathbb{E}_{\mathrm{bulk}}>}. \quad (42)$$

From this analysis, we can expect MK to depend on the orientation dispersion through the dependence of K_{shear} on V_{shear} (Eq. 22), just as FA depends on orientation dispersion [**?**]. This may explain why there is a strong correlation between MK and FA [53]. To obtain a kurtosis metric purely related to microscopic anisotropy that is independent of orientation dispersion, we propose the microscopic kurtosis:

$$K_\mu = \frac{6}{5}\frac{<\langle \mathbf{D}^{\otimes 2}\rangle, \mathbb{E}_{\text{shear}}>}{<\langle \mathbf{D}\rangle^{\otimes 2}, \mathbb{E}_{\text{bulk}}>}. \quad (43)$$

2.7 Estimation of the tensor covariance

To estimate the fourth-order covariance $\mathbb{C}$ from a set of dMRI measurements, we first denote $\mathbb{B} = \mathbf{B}^{\otimes 2}$ and $\mathbb{C}$ in Voigt notation as column vectors of size 21 × 1, represented by $\mathbb{b}$ and $\mathbb{c}$ and we denote $\mathbf{B}$ as a column vector of size 6×1, represented by $\mathbf{b}$. We can now estimate the non-diffusion encoded signal S_0, the average diffusion tensor $\langle \mathbf{d} \rangle$ and the tensor covariance $\mathbb{c}$ by solving the following equation system

$$\begin{pmatrix} \log S_1 \\ \vdots \\ \log S_m \end{pmatrix} = \begin{pmatrix} 1 & -\mathbf{b}_1^{\mathrm{T}} & \frac{1}{2}\mathbb{b}_1^{\mathrm{T}} \\ \vdots & \vdots & \vdots \\ 1 & -\mathbf{b}_m^{\mathrm{T}} & \frac{1}{2}\mathbb{b}_m^{\mathrm{T}} \end{pmatrix} \begin{pmatrix} S_0 & \langle \mathbf{d} \rangle & \mathbb{c} \end{pmatrix}^{\mathrm{T}} \quad (44)$$

$$\underbrace{\mathbf{S}}_{m\times 1} = \underbrace{\mathbf{X}}_{m\times p}\ \underbrace{\boldsymbol{\beta}}_{p\times 1} \quad (45)$$

where $\boldsymbol{\beta}$ is the model parameter vector (S_0 $\langle \mathbf{d} \rangle$ $\mathbb{c}$ containing the estimated non-diffusion encoded signal, the mean of the diffusion tensor distribution (a diffusion tensor), and its variance (a 4th-order covariance tensor), and where m is the number of measurements and p is the number of parameters of the model ($p = 1 + 6 + 21 = 28$). The $\boldsymbol{\beta}$ vector can be estimated by pseudoinversion according to

$$\boldsymbol{\beta}^* = (\underbrace{\mathbf{X}^{\mathrm{T}}\mathbf{X}}_{p\times p})^{-1}\mathbf{X}^{\mathrm{T}}\mathbf{S}. \quad (46)$$

To simplify the description, we omit in this section correction for heteroscedasticity introduced by the logarithmic transformation of the signal data, but we include the correction in the data analysis section below.

For $\mathbf{X}^{\mathrm{T}}\mathbf{X}$ to be invertible, it must have full rank, i.e., rank($\mathbf{X}^{\mathrm{T}}\mathbf{X}$) = 28. Note that 28 = 1+6+21, so this number can intuively be related to the one paramter to specify the signal

baseline, the 6 parameters required to specify the 2nd order mean diffusion tensor, and the 21 parameters needed to specificy the 4th order covariance tensor.

Just as in DTI, which requires sampling in at least 6 “non-collinear” directions, we need to sample with at least 21 unique linear combinations of $\mathbb{b}$ to estimate $\mathbb{c}$. To formally specify the requirements on these measurements is beyond the scope of this work, but we here provide a rule of thumb similar to the useful albeit incomplete “non-collinear” requirement in DTI [54]. First, note that with SDE encoding, the b-tensor has rank-1 and can only have a stick shape. As a consequence, the rank of $\mathbf{X}^{\mathrm{T}}\mathbf{X}$ is limited to $p = 1 + 6 + 15 = 22$. This is since $\mathbb{B} = b^2\mathbf{n}^{\otimes 4} = b^2 n_i n_j n_k n_l$ is fully symmetric, with indices that are fully exchangeable. It is known that fully symmetric 4th order tensors have only 15 unique elements. For experiments performed with b-tensors of rank 2 or 3, however, $\mathbb{B} = \mathbf{B}^{\otimes 2} = b_{ij}\, b_{kl}$, in which case $\mathbb{B}$ has major symmetry and thus up to 21 unique elements. Hence, the rank of $\mathbf{X}^{\mathrm{T}}\mathbf{X}$ can become 1+ 6+ 21 = 28, provided that the signal is sampled using b-tensors with, for example, different shapes, sizes, and orientations. Figure 6 demonstrates that sampling with different shapes (e.g. linear, planar and isotropic) and sizes (i.e. b-values) of the b-tensor disentangles the three cases shown in Fig. 1, which are indistinguishable with SDE only (green lines).

3 Method

3.1 Implementation

We acquired data for q-space trajectory imaging (QTI) on a clinical MRI scanner (Philips Achieva 3T) using a pulse sequence developed in house adapted from [9]. Imaging parameters were: TE = 160 ms, TR = 6000 ms, field of view = 288×288×60 mm^3, image resolution 3 × 3 × 3 mm^3, partial Fourier factor of 0.8. Diffusion encoding was performed using q-space trajectory encoding waveforms. Identical waveforms were executed before and after the 180° pulse to compensate for potential non-linear gradient terms. The gradient waveforms were designed using Eq. 4 (Figure 4).

We implemented two acquisition schemes: a preliminary acquisition and a proof-of-principle scheme designed for clinical studies. The preliminary acquisition had 11 linearly spaced b-values between 50 and 2000 s/mm^2, using linear, prolate, spherical, oblate and planar b-tensors, rotated into the six directions specified by the icosahedral direction scheme (Figure 7), yielding in total 330 measurements. The clinical acquisition protocol was composed of 216 measurements and utilized five b-values. Measurement tensors of four shapes were employed, i.e., sticks, prolates, spheres, and planes, each associated with a specific gradient trajectory (Table 2). From 6 to 30 b-tensor “measurement directions” were obtained by rotating the gradient waveforms using an evenly distributed geometric sampling scheme (Figure 7).

3.2 Subjects

Five patients with schizophrenia and five age-matched healthy controls without neurological disorders were investigated using the clinical protocol. The local institutional review board approved all study protocols and written informed consent was obtained from all subjects. All schizophrenia patients met the DSM-5 criteria for schizophrenia. Disease duration was

between 5 and 12 years (median of 10 years). The median Positive and Negative Syndrome Scale score at the time of MRI was 55, with a range of 42–71.

3.3 Analysis

Data was motion-corrected with affine transforms optimizing the mutual information between acquired data and reference volumes extrapolated from low b-value volumes [56]. Optimization was performed using three degrees of freedom: rotation around the z-axis and in-plane translations, i.e., along the x- and y-directions.

The average diffusion tensor and the tensor covariance were fitted to the data using Eq. 44. Prior to fitting, data was smoothed using a Gaussian filter with a standard deviation of 0.5 voxels. The fit was corrected for heteroscedasticity using $\mathbf{HS} = \mathbf{HX}\boldsymbol{\beta}$ as the regression model instead of $\mathbf{S} = \mathbf{X}\boldsymbol{\beta}$, where $\mathbf{H}$ is a diagonal matrix with the signal amplitudes as diagonal elements [57]. Scalar maps derived from the QTI framework representing the mean and variance of the DTD, i.e., MD, V_{MD}, V_{shear}, and V_{iso}, were calculated from Eqs. 14, 19, 22, and 26. Normalized variance measures, i.e., C_{MD}, C_{μ}, C_{M} and C_{c} were calculated by using Eqs. 27, 28, 30, and 33. Kurtosis maps were calculated by using Eqs. 37, 41, 42, and 43.

FA maps were registered to MNI space using [58]. ROIs for global white matter (WM) were defined in template space from the Harvard-Oxford atlas and projected to subject space to extract values for analysis and group comparisons. Only voxels present in all subjects were included in the WM mask. Significance was tested using the t-test (two-tailed, assuming equal variances). We refrained from a more detailed and regional analysis due to the limited statistical power offered by the limited group sizes [59].

4 Results

We first present the preliminary data, followed by the clinical pilot study. Preliminary data was acquired with five different shapes of the diffusion encoding tensor. Despite the rather long echo time (TE = 160 ms) in the prototype implementation, the sequence yielded high quality images even at the maximal diffusion encoding (Fig. 8A). More efficient encoding can be obtained by incorporating a pause for the 180° pulse in the gradient waveform [60], in contrast to the present implementation where the same waveform was applied before and after the 180° pulse. The dual nature of a linear and planar diffusion encoding is evident in regions of the images with coherent fibers, where structures that appear bright in images encoded with a stick-shaped b-tensor appear dark in those encoded with the planar b-tensor, and vice versa (Fig. 8A) [31, 29]. In white matter, the signal for high b-values decreases as the shape of the b-tensor goes from linear, through prolate to isotropic, but increases again for oblate and planar tensors (see Fig. 8B, corpus callosum and crossing WM). In cortical regions with high fiber orientation dispersion, the signal also varies with the shape of the b-tensor, but to a lesser degree (Fig. 8B). The difference in signal from measurements with differently shaped b-tensors depends on the underlying distribution of microscopic diffusion tensors (Fig. 6).

Figure 9 demonstrates parameter maps from QTI, calculated from data obtained with the clinical protocol. Figure 9A shows the mean and variance of the diffusion tensors, i.e., the

mean diffusivity (MD), the variance of the mean diffusivity, and the shear variance (V_{MD} and V_{shear}). These parameters were obtained by fitting Eq. 13 to the data and calculating invariant projections of the tensors $\langle \mathbf{D} \rangle$ and $\mathbb{C}$ using Eqs. 14, 19, and 22. As expected, the map of MD is high in the ventricles and the subarachnoid space where there is cerebrospinal fluid, and at its lowest in the white matter. The map of the variance in MD, V_{MD}, exhibits high values in regions where we expect high variability in mean diffusivities, for example, in voxels with both tissue and cerebrospinal fluid. Regions with MD above 2.6 $\mu m^2/ms$ were masked out, since high b-value data were inseparable from the noise floor in such regions. It is noteworthy that V_{MD} is non-zero in most parts of the brain. The map of variance in shape and orientation, V_{shear}, shows low values in gray matter and high values in white matter, with the exception of the corpus callosum where the fibers are more well-aligned than in other structures. The last map of V_{iso} shows the total variance, which is the sum of size, shape, and orientation variance.

Maps of normalized variance measures are presented in Fig. 9B. The measures are the size variance parameters (C_{MD}), the micro- and macroscopic anisotropy parameters ($C_\mu = \mu FA^2$ and $C_M = FA^2$), and the microscopic orientation coherence measure (C_c). The normalized size variance is higher in gray than in white matter. The microscopic anisotropy C_μ is high and relatively uniform in white matter, even in crossing fiber regions, whereas the macroscopic anisotropy is lower in regions of crossing fibers than in single fiber regions. Finally, the orientation coherence C_c is high in larger coherent tracts such as the corpus callosum, and lower in regions of high orientation dispersion.

Figure 9C compares DKI's MK with the kurtosis measures derived from the QTI analysis, which separate the diffusional kurtosis into two components (Eqs. 37, 41, and 42). The conventional diffusional kurtosis MK is generally low in the gray matter and high in the white matter. The kurtosis related to dispersion in mean diffusivity, K_{bulk}, is generally low in the white matter, but higher and uniform in the gray matter. The kurtosis related to the difference between local and global anisotropy, K_{shear}, is high in most of the white matter except in regions of coherent fiber structures such as the corpus callosum. The alternative definition of the anisotropy-related kurtosis in Eq. 43, K_μ, which relates only to anisotropy-induced variance and not to the degree of orientation coherence, is high also in the corpus callosum.

Maps of FA and μFA are presented in Fig. 10. The μFA was calculated from Eq. 28 and corresponds to the value the conventional FA would assume if all fibers were parallel. The parameter is thus independent of the fiber orientation dispersion and shows high values across all WM. In contrast, the FA calculated from $\langle \mathbf{D} \rangle$ using Eq. 30 shows low values in regions of crossing fibers. In fact, the FA map resembles the regularity parameter C_{shear}, calculated by Eq. 32. Hence, FA primarily reflects the degree of order among fibers in white matter and to a lesser degree the amount of microscopic diffusional anisotropy. The features of the μFA map agree well with the in-vivo maps obtained with DDE and qMAS-based approaches in previous studies [9, 51].

4.1 Example clinical study of schizophrenia

To investigate the clinical feasibility of the proposed diffusion MRI framework we performed a small pilot study comparing five healthy controls to five patients with schizophrenia. Due to the small number of subjects, the results from the study are preliminary, and a larger study is planned to confirm the implications of the current findings. Parameter maps were calculated for all subjects, and analyzed using in-house software to obtain an average value across all white matter, as defined from the Harvard-Oxford atlas in template space and backprojected to subject space.

Table 3 shows a comparison of parameters between white matter of controls and patients with schizophrenia. Although the statistical power was limited due to the small group sizes ($n = 5$), we note that significant differences between the groups were found for eight of eleven parameters tested. Patients had significantly higher MD and V_{MD}, whereas no effect was found for V_{shear} and V_{iso}. The normalized variances C_{μ} and C_{M} showed significance. The four normalized parameters are plotted in Fig. 11, showing a separation between the groups especially for C_{μ}. Both anisotropy measures μFA and FA were significantly lower in the patients. For kurtosis, the conventional MK showed no difference, whereas all the more specific kurtosis metrics showed significant differences, with higher K_{bulk} and lower K_{shear} and K_{μ} in the patients.

Previous studies suggest that two separate pathologies dominate changes seen in schizophrenia by diffusion MRI [62]: cellular pathology (likely demyelination) and increased levels of extracellular free water (attributed to atrophy or to neuroinflammation), see Fig. 12. We tested these hypotheses by comparing analysis of simulated data with average WM data from our study. For demyelination, we simulated measurements on a group of parallel fibers with varying radial diffusivity (RD) while keeping the axial diffusivity (AD) fixed (AD = 2.6 $\mu m^2/ms$, RD = 0.05 $\rightarrow$ 1.7 $\mu m^2/ms$), inspired by [63]. For the free water hypothesis, we simulated measurements on dispersed fibers with AD = 2.0 $\mu m^2/ms$ and RD = 0.2 $\mu m^2/ms$ being gradually replaced with isotropic water with MD = 2.9 $\mu m^2/ms$. The values of these parameters are in agreement with what can be expected for white matter in general [64] and were slightly adjusted to improve agreement between simulated and observed values. Note that this model is simplistic, but can nevertheless illustrate potential mechanisms of change that can be separated by the DTD model.

The data from average white matter did not agree well with the predictions of the demyelination hypothesis (red lines), here modeled by a coherent increase in the radial diffusivity of fibers. For the free water hypothesis, however, here modeled by replacing fibers with an isotropic diffusion component, the agreement was good (blue lines). These results suggest that most of the effect in the schizophrenia group is driven by an increase in both MD and V_{MD} resulting from increased levels of free water. The increase in these parameters may also be responsible for the reductions of the apparent anisotropies FA and μFA, through an increase in the denominators of Eqs. 30 and 28.

5 Discussion

In this work, we have introduced QTI and expanded the diffusion signal by the cumulant to the fourth order to enable identification of the fourth-order covariance term in the tensor distribution [36]. Thus, the tensor $\mathbb{C}$ has a simple interpretation as the covariance of "local" diffusion tensors.

Other studies have also explored the use of fourth-order tensors. DKI is directly related to the cumulant expansion of the diffusion-encoded signal [35]. QTI and DKI both provide quantitative measures, but QTI is more specific since DKI entangles the two isotropic components of the fourth-order tensor (Fig. 1, Eqs. 40–43). We would like to stress that the different types of diffusion tensor covariances cannot be estimated using only rank-1 b-tensors. The fourth order covariance matrix carries unique information in its two isotropic components, of which one relates to microscopic anisotropy. In the context of DDE, fourth-order tensor models have been used extensively. For example, Lawrence et al. derived such a model based on a Taylor expansion of the MR signal [38], while Jespersen et al. investigated the cumulant expansion [39]. Jensen et al. developed a dPFG version of DKI, that involved a fourth-order tensor with 66 unique elements [65]. Distinct advantages of the framework we propose are 1) that it is applicable to arbitrary gradient encoding schemes, 2) the complex diffusion measurements have an intuitive geometric meaning, and 3) the analysis produces an output that has a simple interpretation: mean and covariance of a tensor distribution.

By generalizing the concept of diffusion encoding in our analysis, we do not need to be limited by traditional PFG-type encoding. To analyze diffusion encoding performed with arbitrary gradient waveforms, we express the diffusion encoding in terms of a general measurement b-tensor. Although the b-matrix concept is well established and can be found in standard text books on diffusion NMR and MRI [41, 42, 1, 43], the characterization of the b-matrix using DDE and more general gradient waveform diffusion MRI is a novel concept. In current literature, the concept of the b-matrix normally refers to the standard rank-one measurement (in our terminology) with added imaging gradient and other correction terms. Extending the traditional rank-1 diffusion measurement, to both rank-2 and full rank-3 measurements, allows measurement of information that is not attainable with SDE measurements.

In the present imaging protocol, the imaging voxels were also relatively large ($3\times3\times3$ mm^3) due to the long echo time (TE = 160 ms) necessitated by the present prototype-like implementation on the MRI scanner. We are confident that considerably improved implementations are possible, and that the protocol settings can be optimized using established methods [66]. A minimal requirement for a protocol, however, is that data is acquired with measurement tensors of varying shapes, which is not possible with SDE only. By optimizing parameter settings, we believe that standard DTI resolutions will be obtainable in clinically relevant imaging times.

Numerous DTI studies have shown that FA is a sensitive parameter, but that it lacks specificity. For example, crossing fibers result in lower FA and will be seen as a variation of FA in white matter [8, 9]. By contrast, C_μ (or μFA) displays little variation within the white

matter, which is an important feature of C_μ since any disease-related reduction of the microscopic anisotropy will stand out clearly and be specific in terms of microstructure. Since white matter exhibits some degree of orientation dispersion [67, 68, 47], we recommend the use of C_μ (or μFA) for analysis of white matter microstructure rather than the conventional FA, which entangles orientation dispersion and microscopic anisotropy into a single metric. Many studies have also shown that MD is very sensitive to changes in cell density, useful for example in tumor diagnosis [69]. Due to the random ordering of tumor cells, FA is of little use for understanding tumor microstructure, whereas μFA can enable non-invasive quantification of average cell shape [70, 9].

The application of QTI in schizophrenia patients generated a number of noteworthy observations. As expected [62], the chronic schizophrenia patients showed elevated MD in the white matter. Interestingly, this increase was matched by an increase in V_{MD}. This increase cannot be explained by a homogeneous increase in the local mean diffusivity, but can be explained by an increasing fraction of free water (Fig. 12). This suggests that increased extracellular water, e.g., due to chronic neuroinflammatory processes or atrophy, is the primary mechanism explaining white matter diffusion changes in our cohort of patients with chronic schizophrenia [71]. However, we also observed reduced C_μ but unchanged C_c in the schizophrenia patients, which could indicate axonal degradation at a microscopic level. Further studies with larger sample sizes are needed to confirm these findings. We note that the current results, obtained by averaging throughout the entire white matter, do not lend themselves to the precise interpretation of the newly proposed measures in comparison with more traditional SDE measures. It will be interesting and more meaningful to study localized changes in both the white matter and the gray matter, and then to assess these results with analogy to simple prototype distributions, such as those in Figure 5.

The results from our pilot study are preliminary because of the low number of subjects (5+5). By comparing measures from the subjects with those obtained from simulations of two different pathologies, we were able to show that diffusion changes occurring in schizophrenia are best explained by an increasing fraction of free water. This suggests that increased levels of extracellular water, e.g. due to chronic neuroinflammatory processes or atrophy, are the primary mechanism explaining white matter diffusion changes in our cohort of patients with chronic schizophrenia. However, further studies with larger sample sizes are needed to validate this finding. Larger sample sizes would also be required to separate global and local effects, especially considering that it is not known whether global effects precede local alterations [62].

The proposed framework has some noteworthy limitations. First, the present analysis assumes Gaussian diffusion in each microenvironment. We believe that this is a relevant starting point for analysis of diffusion MRI data from white matter obtained with clinical MRI scanners, since with limited hardware, the time during which the diffusion is encoded is far longer than the characteristic time scale where the diffusion process turns from being free to restricted [72]. For example, most axons in the corpus callosum are below 2–3 μm [73]. Assuming an intrinsic intra-axonal diffusivity of 2 μm^2/ms, the characteristic time scale is 2–4 ms. Here, we performed diffusion encoding during approximately 100 ms, and thus the radial diffusion coefficient of white matter was likely nearly zero. This means that the

assumption of Gaussian diffusion in each local domain is reasonable. This is also the starting point for model-based methods such as NODDI [47]. Under the assumption of Gaussian diffusion in each microenvironment, any q-space trajectory that produces a specific **B** will be equal. If we want to include restricted diffusion effects in the model, our current second-order model of the q-space trajectory would need to be extended.

Other aspects that may be important to consider are water exchange and coherent flow. At least in healthy white matter, water exchange likely takes place on time scales much longer than the duration of the diffusion encoding [72]. Coherent flow would result in a dependence of the MR signal on the amount by which the encoding is flow compensated [74, 75]. Extending the signal model to account for restricted diffusion, water exchange and coherent flow was, however, beyond the scope of the present work. Another limitation is the approximation in Eq. 12, which is only valid for b-values up to the convergence radius [48]. Estimates of C_{μ} will suffer from systematic errors if the maximum b-value is too large. However, this is a limitation that is also shared with other models based on the cumulant expansion, such as DTI and DKI, and the specific impact on QTI parameters will be addressed in future research. Another potential source of bias is low SNR for high b-value acquisitions and the rectified noise floor that results from it [76]. This problem is also present for SDE and can be met by adjusting the voxel size. For QTI, optimized gradient waveforms can also contribute to substantially improved SNR by reduced TE [60].

6 Conclusions

We have described a new diffusion MR framework for imaging and modeling of microstructure that we call q-space trajectory imaging. Our work shows that performing diffusion encoding with a wide range of q-space trajectories is feasible on a clinical system. The work further generalizes the concept of b-values, enabling new types of measurements not available with conventional SDE-based diffusion MRI. We showed that the cumulant expansion of the MR signal yields the mean diffusion tensor and a fourth-order covariance tensor. While the diffusion tensor is represented by a single isotropic parameter (MD), the covariance tensor is characterized by two principal isotropic parameters, i.e., V_{MD} and V_{shear}, that represent within-voxel variance of diffusion coefficients. Together with the diffusion tensor, these parameters can be used to disentangle the diffusional kurtosis into more specific representations, or to calculate parameters such as C_{MD}, C_{μ} and C_{c}. These parameters are more specific than what is possible to obtain with conventional DTI and DKI. By disentangling variation in size from variation in shape and direction, our framework may be useful for studying changes beyond the macroscopic anisotropy as is done with conventional DTI. Alterations in macroscopically isotropic regions, where there is high orientation dispersion or low microscopic anisotropy but variance in size, could be captured by our new normalized variance measures. Since the framework does not require macroscopic anisotropy, our framework could be useful not only in white matter but also in gray matter.

Acknowledgments

The authors acknowledge the NIH grants R01MH074794, R01MH092862, R01MH102377, R01AG042512, P41EB015902, P41EB015898, U01CA199459, and the Swedish Research Council (VR) grants 2012-3682,

2011-5176, 2014-3910, TÜBITAK-EU COFUND project no. 114C015, and Swedish Foundation for Strategic Research (SSF) grant AM13-0090.

References

1. Callaghan, PT. Translational dynamics and magnetic resonance: principles of pulsed gradient spin echo NMR. Oxford University Press; 2011.
2. Stejskal EO, Tanner JE. Spin diffusion measurements: Spin echoes in the presence of a time-dependent field gradient. J Chem Phys. 1965; 42(1):288–292.
3. Basser PJ, Pierpaoli C. Microstructural and physiological features of tissues elucidated by quantitative-diffusion-tensor MRI. J Magn Reson, Series B. 1996; 111(3):209–219.
4. Tuch DS. Q-ball imaging. Magn Reson Med. 2004; 52(6):1358–1372. [PubMed: 15562495]
5. Assaf Y, Blumenfeld-Katzir T, Yovel Y, Basser PJ. AxCaliber: a method for measuring axon diameter distribution from diffusion MRI. Magn Reson Med. 2008; 59(6):1347–1354. [PubMed: 18506799]
6. Nilsson M, van Westen D, Ståhlberg F, Sundgren PC, Lätt J. The role of tissue microstructure and water exchange in biophysical modelling of diffusion in white matter. Magn Reson Mater Phy. 2013; 26(4):345–370.
7. Assaf Y, Pasternak O. Diffusion tensor imaging (DTI)-based white matter mapping in brain research: a review. Journal of molecular neuroscience. 2008; 34(1):51–61. [PubMed: 18157658]
8. Alexander AL, Hasan KM, Lazar M, Tsuruda JS, Parker DL. Analysis of partial volume effects in diffusion-tensor MRI. Magn Reson Med. 2001; 45(5):770–780. [PubMed: 11323803]
9. Szczepankiewicz F, Lasič S, van Westen D, Sundgren PC, Englund E, Westin CF, Ståhlberg F, Lätt J, Topgaard D, Nilsson M. Quantification of microscopic diffusion anisotropy disentangles effects of orientation dispersion from microstructure: Applications in healthy volunteers and in brain tumors. NeuroImage. 2015
10. Bihan DL, Johansen-Berg H. Diffusion MRI at 25: exploring brain tissue structure and function. 2012
11. Jones DK, Knosche TR, Turner R. White matter integrity, fiber count, and other fallacies: the dos and donts of diffusion MRI. 2013
12. Vos SB, Jones DK, Jeurissen B, Viergever M, Leemans A. The influence of complex white matter architecture on the mean diffusivity in diffusion tensor MRI of the human brain. 2012
13. O'Donnell LJ, Pasternak O. Does diffusion MRI tell us anything about the white matter? An overview of methods and pitfalls. Schizophrenia research. 2015; 161(1):133–141. [PubMed: 25278106]
14. Lasič S, Szczepankiewicz F, Eriksson S, Nilsson M, Topgaard D. Microanisotropy imaging: quantification of microscopic diffusion anisotropy and orientational order parameter by diffusion MRI with magic-angle spinning of the q-vector. Font Phys. 2014; 2(11)
15. Özarslan E, Basser PJ. Microscopic anisotropy revealed by NMR double pulsed field gradient experiments with arbitrary timing parameters. J Chem Phys. 2008; 128:154511–11. [PubMed: 18433239]
16. Nilsson M, Lätt J, van Westen D, Brockstedt S, Lasiè S, Ståhlberg F, Topgaard D. Noninvasive mapping of water diffusional exchange in the human brain using filter-exchange imaging. Magnetic Resonance in Medicine. 2013; 69(6):1572–1580.
17. Cory DG, Garriway AN, Miller JB. Applications of spin transport as a probe of local geometry. Polym Prepr. 1990; 31:149–150.
18. Mitra PP. Multiple wave-vector extensions of the NMR pulsed-field-gradient spin-echo diffusion measurement. Phys Rev B. 1995; 51(21):15074.
19. Callaghan P, Komlosh M. Locally anisotropic motion in a macroscopically isotropic system: displacement correlations measured using double pulsed gradient spin-echo NMR. Magnetic Resonance in Chemistry. 2002; 40(13):S15–S19.
20. Lasiè S, Nilsson M, Lätt J, Ståhlberg F, Topgaard D. Apparent exchange rate mapping with diffusion MRI. Magn Reson Med. 2011; 66(2):356–365. [PubMed: 21446037]

21. Wong EC, Cox RW, Song AW. Optimized isotropic diffusion weighting. Magnetic Resonance in Medicine. 1995; 34(2):139–143. [PubMed: 7476070]
22. Valette J, Giraudeau C, Marchadour C, Djemai B, Geffroy F, Ghaly MA, Le Bihan D, Hantraye P, Lebon V, Lethimonnier F. A new sequence for single-shot diffusion-weighted NMR spectroscopy by the trace of the diffusion tensor. Magn Reson Med. 2012; 68(6):1705–1712. [PubMed: 22302673]
23. Topgaard D. Isotropic diffusion weighting using a triple-stimulated echo pulse sequence with bipolar gradient pulse pairs. Microporous and Mesoporous Materials. 2015; 205:48–51.
24. Eriksson S, Lasič S, Nilsson M, Westin CF, Topgaard D. NMR diffusion-encoding with axial symmetry and variable anisotropy: Distinguishing between prolate and oblate microscopic diffusion tensors with unknown orientation distribution. J Chem Phys. 2015; 142(10):104201. [PubMed: 25770532]
25. Shemesh N, Jespersen SN, Alexander DC, Cohen Y, Drobnjak I, Dyrby TB, Finsterbusch J, Koch MA, Kuder T, Laun F, Lawrenz M, Lundell H, Mitra PP, Nilsson M, Özarslan E, Topgaard D, Westin CF. Conventions and nomenclature for double diffusion encoding (DDE) NMR and MRI. Magnetic Resonance in Medicine. 2016; 75(1):82–87. [PubMed: 26418050]
26. Does MD, Parsons EC, Gore JC. Oscillating gradient measurements of water diffusion in normal and globally ischemic rat brain. Magn Reson Med. 2003; 49(2):206–215. [PubMed: 12541239]
27. Drobnjak I, Alexander DC. Optimising time-varying gradient orientation for microstructure sensitivity in diffusion-weighted MR. J Magn Reson. 2011; 212(2):344–354. [PubMed: 21889378]
28. Lundell H, Snderby CK, Dyrby TB. Diffusion weighted imaging with circularly polarized oscillating gradients. Magnetic Resonance in Medicine. 2015; 73(3):1171–1176. [PubMed: 24639209]
29. Özarslan E, Avram AV, Basser PJ, Westin CF. Rotating field gradient (RFG) MR for direct measurement of the diffusion orientation distribution function (dODF). ISMRM 2014. 2014
30. Eriksson S, Lasič S, Topgaard D. Isotropic diffusion weighting in PGSE NMR by magic-angle spinning of the q-vector. J Magn Reson. 2013; 226:13–18. [PubMed: 23178533]
31. Westin CF, Nilsson M, Szczepankiewicz F, Pasternak O, Özarslan E, Topgaard D, Knutsson H. In-vivo diffusion q-space trajectory imaging. ISMRM 2014. 2014
32. Ernst, RR.; Bodenhausen, G.; Wokaun, A., et al. Principles of nuclear magnetic resonance in one and two dimensions. Vol. 14. Clarendon Press Oxford; 1987.
33. Siria A, Poncharal P, Biance AL, Fulcrand R, Blase X, Purcell ST, Bocquet L. Giant osmotic energy conversion measured in a single transmembrane boron nitride nanotube. Nature. 2013; 494(7438):455–458. [PubMed: 23446417]
34. Liu C, Bammer R, Acar B, Moseley ME. Characterizing non-Gaussian diffusion by using generalized diffusion tensors. Magn Reson Med. 2004; 51(5):924–937. [PubMed: 15122674]
35. Jensen JH, Helpern JA, Ramani A, Lu H, Kaczynski K. Diffusional kurtosis imaging: the quantification of non-gaussian water diffusion by means of magnetic resonance imaging. Magn Reson Med. 2005; 53(6):1432–1440. [PubMed: 15906300]
36. Basser PJ, Pajevic S. Spectral decomposition of a 4th-order covariance tensor: Applications to diffusion tensor MRI. Signal Processing. 2007; 87(2):220–236.
37. Jian, B.; Vemuri, BC. Information Processing in Medical Imaging. Springer; 2007. Multi-fiber reconstruction from diffusion MRI using mixture of Wisharts and sparse deconvolution; p. 384-395.
38. Lawrenz M, Koch MA, Finsterbusch J. A tensor model and measures of microscopic anisotropy for double-wave-vector diffusion-weighting experiments with long mixing times. J Magn reson. 2010; 202(1):43–56. [PubMed: 19854085]
39. Jespersen SN, Lundell H, Sønderby CK, Dyrby TB. Orientationally invariant metrics of apparent compartment eccentricity from double pulsed field gradient diffusion experiments. NMR Biomed. 2013; 26(12):1647–1662. [PubMed: 24038641]
40. Westin, CF.; Szczepankiewicz, F.; Pasternak, O.; Özarslan, E.; Topgaard, D.; Knutsson, H.; Nilsson, M. Medical Image Computing and Computer-Assisted Intervention–MICCAI 2014. Springer; 2014. Measurement tensors in diffusion MRI: generalizing the concept of diffusion encoding; p. 209-216.

41. Karlicek R, Lowe I. A modified pulsed gradient technique for measuring diffusion in the presence of large background gradients. Journal of Magnetic Resonance (1969). 1980; 37(1):75–91.
42. Mattiello J, Basser PJ, Le Bihan D. The b matrix in diffusion tensor echo-planar imaging. Magnetic Resonance in Medicine. 1997; 37(2):292–300. [PubMed: 9001155]
43. Price, WS. NMR studies of translational motion: principles and applications. Cambridge University Press; 2009.
44. Basser PJ, Jones DK. Diffusion-tensor MRI: theory, experimental design and data analysis - a technical review. NMR Biomed. 2002; 15(7–8):456–467. [PubMed: 12489095]
45. Andrew ER, Bradbury A, Eades RG. Removal of dipolar broadening of nuclear magnetic resonance spectra of solids by specimen rotation. Nature. 1959; 183:1802–1803.
46. Topgaard D, Söderman O. Experimental determination of pore shape and size using q-space NMR microscopy in the long diffusion-time limit. Magnetic resonance imaging. 2003; 21(1):69–76. [PubMed: 12620549]
47. Zhang H, Schneider T, Wheeler-Kingshott CA, Alexander DC. NODDI: practical in vivo neurite orientation dispersion and density imaging of the human brain. NeuroImage. 2012; 61(4):1000–1016. [PubMed: 22484410]
48. Kiselev VG, Il'yasov KA. Is the "biexponential diffusion" biexponential? Magn Reson Med. 2007; 57(3):464–469. [PubMed: 17326171]
49. Moakher M. Fourth-order cartesian tensors: old and new facts, notions and applications. The Quart Jour of Mechanics and Applied Math. 2008; 61(2):181–203.
50. Westin, CF.; Nilsson, M.; Pasternak, O.; Knutsson, H. Diffusion tensors from double-PFG of the human brain. The International Society for Magnetic Resonance in Medicine; 21st Annual Meeting & Exhibition (ISMRM 2013); 20–26 April 2013; Salt Lake City, Utah, USA. 2013.
51. Lawrenz M, Finsterbusch J. Double-wave-vector diffusion-weighted imaging reveals microscopic diffusion anisotropy in the living human brain. Magnetic Resonance in Medicine. 2013; 69(4): 1072–1082. [PubMed: 22711603]
52. Hansen B, Lund TE, Sangill R, Jespersen SN. Experimentally and computationally fast method for estimation of a mean kurtosis. Magn Reson Med. 2013; 69(6):1754–1760. [PubMed: 23589312]
53. Lätt J, Nilsson M, Wirestam R, Ståhlberg F, Karlsson N, Johansson M, Sundgren PC, van Westen D. Regional values of diffusional kurtosis estimates in the healthy brain. J Magn Reson Imag. 2013; 37(3):610–618.
54. Özcan A. (mathematical) necessary conditions for the selection of gradient vectors in DTI. Journal of Magnetic Resonance. 2005; 172:238–241. [PubMed: 15649751]
55. Westin, CF.; Pasternak, O.; Knutsson, H. Rotationally invariant gradient schemes for diffusion MRI. Proceedings of the ISMRM Annual Meeting (ISMRM'12); May 2012;
56. Nilsson M, Szczepankiewicz F, van Westen D, Hansson O. Extrapolation-Based References Improve Motion and Eddy-Current Correction of High B-Value DWI Data: Application in Parkinson's Disease Dementia. PLoS One. 2015; 10(11):e0141825. [PubMed: 26528541]
57. Jones DK, Cercignani M. Twenty-five pitfalls in the analysis of diffusion MRI data. NMR Biomed. 2010; 23(7):803–820. [PubMed: 20886566]
58. Jenkinson M, Beckmann CF, Behrens TE, Woolrich MW, Smith SM. FSL. Neuroimage. 2012; 62(2):782–790. [PubMed: 21979382]
59. Szczepankiewicz F, Lätt J, Wirestam R, Leemans A, Sundgren PC, van Westen D, Ståhlberg F, Nilsson M. Variability in diffusion kurtosis imaging: impact on study design, statistical power and interpretation. NeuroImage. 2013; 76:145–154. [PubMed: 23507377]
60. Sjölund J, Szczepankiewicz F, Nilsson M, Topgaard D, Westin CF, Knutsson H. Constrained optimization of gradient waveforms for generalized diffusion encoding. J Magn Reson. 2015; 261
61. Tuch DS. Q-ball imaging. Magnetic Resonance in Medicine. 2004; 52(6):1358–1372. [PubMed: 15562495]
62. Pasternak O, Westin CF, Bouix S, Seidman LJ, Goldstein JM, Woo TUW, Petryshen TL, Mesholam-Gately RI, McCarley RW, Kikinis R, et al. Excessive extracellular volume reveals a neurodegenerative pattern in schizophrenia onset. The Journal of Neuroscience. 2012; 32(48): 17365–17372. [PubMed: 23197727]

63. Song SK, Sun SW, Ramsbottom MJ, Chang C, Russell J, Cross AH. Dysmyelination revealed through MRI as increased radial (but unchanged axial) diffusion of water. Neuroimage. 2002; 17(3):1429–1436. [PubMed: 12414282]
64. Pierpaoli C, Jezzard P, Basser PJ, Barnett A, Di Chiro G. Diffusion tensor mr imaging of the human brain. Radiology. 1996; 201(3):637–648. [PubMed: 8939209]
65. Jensen JH, Hui ES, Helpern JA. Double-pulsed diffusional kurtosis imaging. NMR Biomed. 2014
66. Alexander DC. A general framework for experiment design in diffusion MRI and its application in measuring direct tissue-microstructure features. Magn Reson Med. 2008; 60(2):439–448. [PubMed: 18666109]
67. Ronen I, Budde M, Ercan E, Annese J, Techawiboonwong A, Webb A. Microstructural organization of axons in the human corpus callosum quantified by diffusion-weighted magnetic resonance spectroscopy of N-acetylaspartate and post-mortem histology. Brain structure & function. 2013
68. Nilsson M, Lätt J, Ståhlberg F, van Westen D, Hagslätt H. The importance of axonal undulation in diffusion MR measurements: a monte carlo simulation study. NMR Biomed. 2012; 25(5):795–805. [PubMed: 22020832]
69. Padhani AR, Liu G, Koh DM, Chenevert TL, Thoeny HC, Takahara T, Dzik-Jurasz A, Ross BD, Van Cauteren M, Collins D, Hammoud DA, Rustin GJS, Taouli B, Choyke PL. Diffusion-weighted magnetic resonance imaging as a cancer biomarker: consensus and recommendations. Neoplasia. 2009; 11(2):102–125. [PubMed: 19186405]
70. Özarslan E. Compartment shape anisotropy (CSA) revealed by double pulsed field gradient MR. Journal of Magnetic Resonance. 2009; 199(1):56–67. [PubMed: 19398210]
71. Pasternak O, Westin CF, Dahlben B, Bouix S, Kubicki M. The extent of diffusion MRI markers of neuroinflammation and white matter deterioration in chronic schizophrenia. Schizophrenia research. 2014
72. Nilsson M, Lätt J, van Westen D, Brockstedt S, Lasiè S, Ståhlberg F, Topgaard D. Noninvasive mapping of water diffusional exchange in the human brain using filter-exchange imaging. Magn Reson Med. 2013; 69(6):1573–1581. [PubMed: 22837019]
73. Aboitiz F, Scheibel AB, Fisher RS, Zaidel E. Fiber composition of the human corpus callosum. Brain Research. 1992; 598(1–2):143–153. [PubMed: 1486477]
74. Turner R, Le Bihan D, Maier J, Vavrek R, Hedges LK, Pekar J. Echo-planar imaging of intravoxel incoherent motion. Radiology. 1990; 177(2):407–414. [PubMed: 2217777]
75. Wetscherek A, Stieltjes B, Laun FB. Flow-compensated intravoxel incoherent motion diffusion imaging. Magn Reson Med. 2014
76. Lätt J, Nilsson M, Malmborg C, Rosquist H, Wirestam R, Ståhlberg F, Topgaard D, Brockstedt S. Accuracy of q-space related parameters in MRI: simulations and phantom measurements. IEEE transactions on medical imaging. 2007; 26(11):1437–1447. [PubMed: 18041259]

7 Appendix

7.1 Vector and matrix notation of higher order tensors

We represented tensors by vectors and matrices in order to simplify implementation in software. A symmetric second-order tensor can be represented by a 6 × 1 column vector according to

$$\mathbf{d}=(\ D_{xx}\quad D_{yy}\quad D_{zz}\quad \sqrt{2}D_{yz}\quad \sqrt{2}D_{xz}\quad \sqrt{2}D_{xy}.\ )^{\mathrm{T}} \tag{47}$$

and symmetric fourth-order tensor can be represented by a 6 × 6 matrix, for example $\mathbb{B}=\mathbf{B}^{\otimes 2}=\mathbf{b}\mathbf{b}^{\mathrm{T}}$, or by a 21 × 1 column vector according to

$$\underbrace{\mathbf{B}^{\otimes 2}}_{3\times3\times3\times3} = \mathbf{B}\otimes\mathbf{B} \leftrightarrow \underbrace{\mathbb{B}}_{6\times6} \leftrightarrow \underbrace{\mathbb{b}}_{21\times1} = (b_{xx}b_{xx} \quad b_{yy}b_{yy} \quad b_{zz}b_{zz} \quad \ldots$$
$$\sqrt{2}\,b_{yy}b_{zz} \;\; \sqrt{2}\,b_{xx}b_{zz} \;\; \sqrt{2}\,b_{xx}b_{yy} \ldots$$
$$\sqrt{4}\,b_{xx}b_{yz} \;\; \sqrt{4}\,b_{xx}b_{xz} \;\; \sqrt{4}\,b_{xx}b_{xy} \ldots$$
$$\sqrt{4}\,b_{yy}b_{yz} \;\; \sqrt{4}\,b_{yy}b_{xz} \;\; \sqrt{4}\,b_{yy}b_{xy} \ldots$$
$$\sqrt{4}\,b_{zz}b_{yz} \;\; \sqrt{4}\,b_{zz}b_{xz} \;\; \sqrt{4}\,b_{zz}b_{xy} \ldots$$
$$\sqrt{4}\,b_{yz}b_{yz} \;\; \sqrt{4}\,b_{xz}b_{xz} \;\; \sqrt{4}\,b_{xy}b_{xy} \ldots$$
$$\sqrt{8}\,b_{yz}b_{xz} \;\; \sqrt{8}\,b_{xz}b_{xy} \;\; \sqrt{8}\,b_{xy}b_{yz})^{\mathrm{T}} \qquad (48)$$

7.2 Inner and outer products

Inner and outer products are simple to implement in software when the tensors are represented by column vectors and matrices. The outer product is then given by

$$\mathbf{D}^{\otimes 2} = \mathbf{d}\mathbf{d}^{\mathrm{T}} \qquad (49)$$

and the inner product by

$$<\mathbf{D},\mathbf{N}> = \mathbf{d}^{\mathrm{T}}\mathbf{n} \qquad (50)$$

and for fourth-order tensors by

$$<\mathbb{D},\mathbb{N}> = \mathbb{d}^{\mathrm{T}}\mathbb{n} \qquad (51)$$

The inner product of two matrices is also defined according to

$$<\mathbf{D},\mathbf{N}> = \mathrm{Tr}(\mathbf{D}\mathbf{N}^{\mathrm{T}}) \qquad (52)$$

We may encounter a case that utilize all of these notations, for example, the evaluation of the square of the apparent diffusion coefficient in the direction ***n***,

$$\mathrm{ADC}^2(\boldsymbol{n}) = <\mathbf{D},\boldsymbol{n}^{\otimes 2}>^2 = <\mathbf{D},\mathbf{N}>^2 = (\mathbf{d}^{\mathrm{T}}\mathbf{n})^2 = \mathbf{d}^{\mathrm{T}}\mathbf{n}\mathbf{n}^{\mathrm{T}}\mathbf{d} = \mathbf{d}^{\mathrm{T}}\mathbb{N}\mathbf{d} =$$
$$= \mathrm{Tr}(\mathbf{d}(\mathbb{N}\mathbf{d})^{\mathrm{T}})) = \mathrm{Tr}((\mathbf{d}\mathbf{d}^{\mathrm{T}})\mathbb{N}^{\mathrm{T}}) = <\mathbb{D},\mathbb{N}> = \mathbb{d}^{\mathrm{T}}\mathbb{n}, \qquad (53)$$

where the following identities follows from the notation

$$\mathbb{N}=\mathbf{n}\mathbf{n}^{\mathrm{T}}=\mathbb{N}^{\otimes 2}=\boldsymbol{n}^{\otimes 4} \quad (54)$$

The above analysis also demonstrates the relation

$$<\mathbf{a},\mathbf{b}>^2=<\mathbf{a}^{\otimes 2},\mathbf{b}^{\otimes 2}>, \quad (55)$$

which becomes important in the analysis of the isotropic bases of the 4th order tensor.

7.3 Isotropic 4th order tensors

First, consider the projection of $\mathbb{C}$ onto $\mathbb{E}_{\text{bulk}}$, using only the rules defined above,

$$\begin{gathered}<\mathbb{C},\mathbb{E}_{\text{bulk}}>=<\langle\mathbf{D}^{\otimes 2}\rangle-\langle\mathbf{D}\rangle^{\otimes 2},\mathbf{E}_{\text{iso}}^{\otimes 2}>= \\ =<\langle\mathbf{D}^{\otimes 2}\rangle,\mathbf{E}_{\text{iso}}^{\otimes 2}>-<\langle\mathbf{D}\rangle^{\otimes 2},\mathbf{E}_{\text{iso}}^{\otimes 2}>= \\ =\langle<\mathbf{D}^{\otimes 2},\mathbf{E}_{\text{iso}}^{\otimes 2}>\rangle-<\langle\mathbf{D}\rangle,\mathbf{E}_{\text{iso}}>^2= \\ =\langle<\mathbf{D},\mathbf{E}_{\text{iso}}>^2\rangle-\langle<\mathbf{D},\mathbf{E}_{\text{iso}}>\rangle^2= \\ =\langle\mathrm{MD}^2\rangle-\langle\mathrm{MD}\rangle^2=V_{\mathrm{MD}}\end{gathered} \quad (56)$$

Second, considering the projection $\mathbf{D}^{\otimes 2}$ on $\mathbb{E}_{\text{shear}}$,

$$\begin{gathered}<\mathbf{D}^{\otimes 2},\mathbb{E}_{\text{shear}}>=<\mathbf{D}^{\otimes 2},\tfrac{1}{3}\mathbb{I}-\mathbf{E}_{\text{iso}}^{\otimes 2}> \\ =<\mathbf{D}^{\otimes 2},\tfrac{1}{3}\mathbb{I}>-<\mathbf{D}^{\otimes 2},\mathbf{E}_{\text{iso}}^{\otimes 2}>= \\ =<\mathbf{D}^2,\mathbf{E}_{\text{iso}}>-<\mathbf{D},\mathbf{E}_{\text{iso}}>^2= \\ =\tfrac{1}{3}\textstyle\sum_{i=1}^3\lambda_i^2-(\tfrac{1}{3}\sum_{i=1}^3\lambda_i)^2=V_\lambda(\mathbf{D})\end{gathered} \quad (57)$$

where we utilized

$$<\mathbf{D}^2,\mathbf{E}_{\text{iso}}>=\tfrac{1}{3}\mathrm{Tr}(\mathbf{D}\mathbf{D})=\tfrac{1}{3}<\mathbf{D},\mathbf{D}>=<\mathbf{D}^{\otimes 2},\tfrac{1}{3}\mathbb{I}> \quad (58)$$

Now we consider projection of $\mathbb{C}$ onto $\mathbb{E}_{\text{shear}}$,

$$\begin{gathered}<\mathbb{C},\mathbb{E}_{\text{shear}}>=<\langle\mathbf{D}^{\otimes 2}\rangle,\mathbb{E}_{\text{shear}}>-<\langle\mathbf{D}\rangle^{\otimes 2},\mathbb{E}_{\text{shear}}>= \\ =\langle<\mathbf{D}^{\otimes 2},\mathbb{E}_{\text{shear}}>\rangle-<\langle\mathbf{D}\rangle^{\otimes 2},\mathbb{E}_{\text{shear}}>= \\ =\langle V_\lambda(\mathbf{D})\rangle-V_\lambda(\langle\mathbf{D}\rangle)\end{gathered} \quad (59)$$

7.4 Cumulant expansion up to six-order tensor

The approximation in Eq. 13 is a cumulant expansion where we expand $s(b) = \log S(b)$ around $b = 0$ according to

$$s(b)=\log\langle\exp(-b<\mathbf{N},\mathbf{D}>)\rangle \approx s(0)+bs^{'}(0)+\tfrac{1}{2}b^{2}s^{''}(0) \quad (60)$$

where

$$s^{'}(b)=\frac{S^{'}(b)}{S(b)} \quad (61)$$

$$s^{''}(b)=\frac{S^{''}(b)}{S(b)}-\left(\frac{S^{'}(b)}{S(b)}\right)^{2} \quad (62)$$

For $b = 0$, these functions evaluate to

$$S(0)=1 \quad (63)$$

$$S^{'}(0)=-\langle<\mathbf{N},\mathbf{D}>\rangle=-<\mathbf{N},\langle\mathbf{D}\rangle> \quad (64)$$

$$S^{''}(0)=\langle<\mathbf{N},\mathbf{D}>^{2}\rangle=\langle<\mathbb{N},\mathbb{D}>\rangle=<\mathbb{N},\langle\mathbb{D}\rangle> \quad (65)$$

where $\mathbb{D}=\mathbf{D}^{\otimes 2}$. Hence $s''(0) =< \mathbb{N}, \langle\mathbf{D}^{\otimes 2}\rangle - \langle\mathbf{D}\rangle^{\otimes 2} >=< \mathbb{N}, \mathbb{C} >$.

Third order term (six-order tensor)

For completeness, we note that

$$s(b) \approx s(0)+b\,s^{'}(0)+\tfrac{1}{2}b^{2}s^{''}(0)-\tfrac{1}{6}b^{3}s^{(3)}(0) \quad (66)$$

where

$$s^{(3)}(b)=\frac{S^{(3)}(b)}{S(b)}-3\frac{S'(b)S''(b)}{S^2(b)}+2\left(\frac{S'(b)}{S(b)}\right)^3 \quad (67)$$

and

$$S^{(3)}(0)=\langle<\mathbf{N},\mathbf{D}>^3\rangle=<\mathbf{N}^{\otimes 3},\langle\mathbf{D}^{\otimes 3}\rangle> \quad (68)$$

so that

$$S^{(3)}(0)=<\mathbf{N}^{\otimes 3},\ \langle\mathbf{D}^{\otimes 3}\rangle-3\langle\mathbf{D}\rangle\otimes\langle\mathbf{D}^{\otimes 2}\rangle+2\langle\mathbf{D}\rangle^{\otimes 3}> \quad (69)$$

where we can define

$$\mathscr{M}=\langle\mathbf{D}^{\otimes 3}\rangle-3\langle\mathbf{D}\rangle\otimes\langle\mathbf{D}^{\otimes 2}\rangle+2\langle\mathbf{D}\rangle^{\otimes 3} \quad (70)$$

and identify $\mathscr{M}$ as the third central moment. This is a rank 6 tensor with 729 elements, of which 56 are unique.

7.5 Taylor expansion

For completeness, we also consider the Taylor expansion of $E(b)$, which is given by

$$S(b)\approx 1-bS'(0)+\frac{b^2}{2}S''(0)=1-<\mathbf{B},\langle\mathbf{D}\rangle>+\frac{1}{2}<\mathbb{B},\langle\mathbb{D}\rangle> \quad (71)$$

The difference is that in the Taylor expansion, which is valid for lower b-values than the Cumulant expansion, the fourth-order term is given by $\langle\mathbb{D}$, whereas it for the cumulant expansion is given by $\mathbb{C}=\langle\mathbb{D}-\langle\mathbf{D}\rangle^{\otimes 2}$.

7.6 Comparison with DKI

For the sake of completeness, we note that the DKI model is given by [35]

$$\log E(b,\boldsymbol{n})=-b<\langle\mathbf{D}\rangle,\boldsymbol{n}^{\otimes 2}>+\frac{b^2}{6}<\langle\mathbf{D}\rangle,\mathbf{E}_{\text{iso}}>^2<\mathbb{W},\boldsymbol{n}^{\otimes 4}>. \quad (72)$$

where $<\langle\mathbf{D}\rangle,\mathbf{E}_{\text{iso}}>=$ MD. Hence

$$\tfrac{1}{3}\mathrm{MD}^2 <\mathbb{W}, \boldsymbol{n}^{\otimes 4}> = <\mathbb{C}, \boldsymbol{n}^{\otimes 4}> \quad (73)$$

Because Eq. 73 involves projection onto outer products of vectors, the following still holds

$$\tfrac{1}{3}\mathrm{MD}^2 \mathbb{W} \neq \mathbb{C} \quad (74)$$

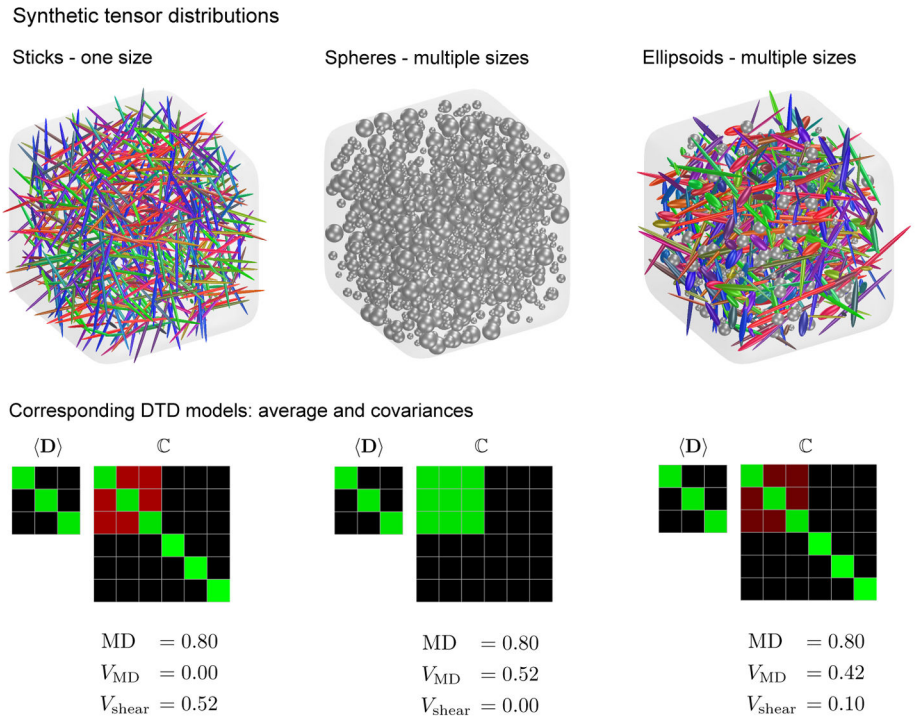

Fig. 1.

Synthetic examples of diffusion tensor distributions that cannot be differentiated using conventional SDE-based dMRI sequences such as DTI, HARDI, DSI, and DKI, but can be distinguished using the proposed QTI framework. The first row shows synthetic examples of diffusion tensor distributions within a voxel that yield an isotropic average diffusion tensor $\langle \mathbf{D} \rangle$. As a consequence, these different structures are indistinguishable with conventional DTI. The second row shows the DTD model corresponding to each synthetic example. The DTD model includes average diffusion tensors, shown by 3×3 matrices, and covariance tensors, shown as 6×6 matrices, along with the scalar invariants from Eqs. 14, 19 and 22. In these graphical representations, green is positive, black is zero, and red is negative. Although the three examples have identical average diffusion tensors they have different covariance tensors $\mathbb{C}$. See the Diffusion and modeling and estimation section (2.3) for details on model estimation. The corresponding fourth-order tensors as observed by diffusional kurtosis imaging using only the linear b-tensors obtained with SDE encoding are equal in these three examples. The ability to measure and model the distribution over diffusion tensors, rather than a quantity that has already been averaged within a voxel, has the potential to provide a powerful new paradigm for the study of complex tissue architecture.

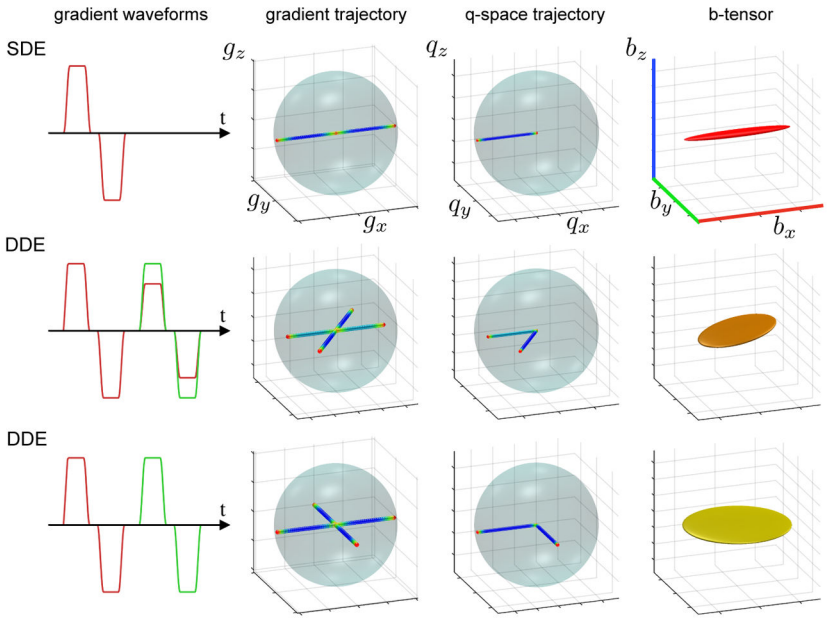

Fig. 2.

Examples of gradient waveforms and trajectories that produce “linear” and “planar” b-tensor shapes, from the SDE and DDE experiments. Color coding is as follows: in the gradients waveform column, red-green-blue defines the x-y-z gradient directions; in the gradient trajectory column, slewrate, slow to fast, is encoded by red-yellow-green-blue from zero to max; in the q-space trajectory column, trajectory speed, slow to fast, is encoded red-yellow-green-blue; in the b-tensor column, the diagonal elements of the b-tensor are mapped to red-green-blue. In the rank-1 case, this b-tensor color mapping corresponds to the principal eigenvector direction, analogous to the standard color coding for diffusion tensors. In the planar case, rather than relying on a randomly oriented major eigenvector for color information, the effect is to sum the colors in the plane (as in the bottom row where red plus green gives yellow in the RGB sense).

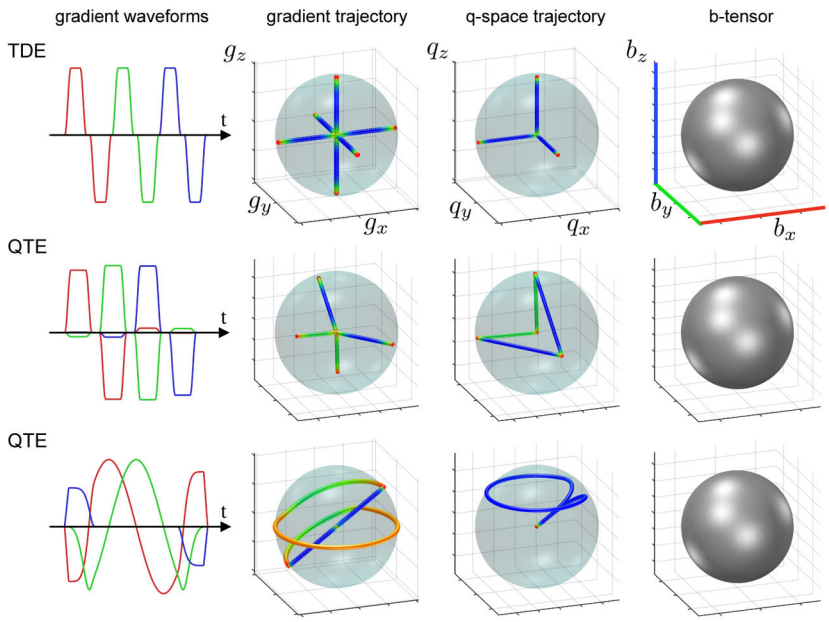

Fig. 3.

TDE and QTE encoding schemes can be used to produce isotropic diffusion encoding, with a spherical b-tensor. Color coding is as follows: in column 1, red-green-blue defines the x-y-z gradient directions; in columns 2 and 3, slewrate and trajectory speed are encoded by red-yellow-green-blue, where red is slow and blue is fast; in column 4 the diagonal elements of the b-tensor are mapped to red-green-blue (and thus gray indicates these elements of the isotropic b-tensor are the same). The encoding scheme in the second row was generated by transforming the TDE encoding from the top row: first, pulses were shifted closer together so the green positive pulse aligned with the negative red pulse etc., and then a transform was applied to make the encoding isotropic, as in Eq. 5. In the bottom row, the isotropic diffusion encoding from qMAS produces a lasso-like q-space trajectory.

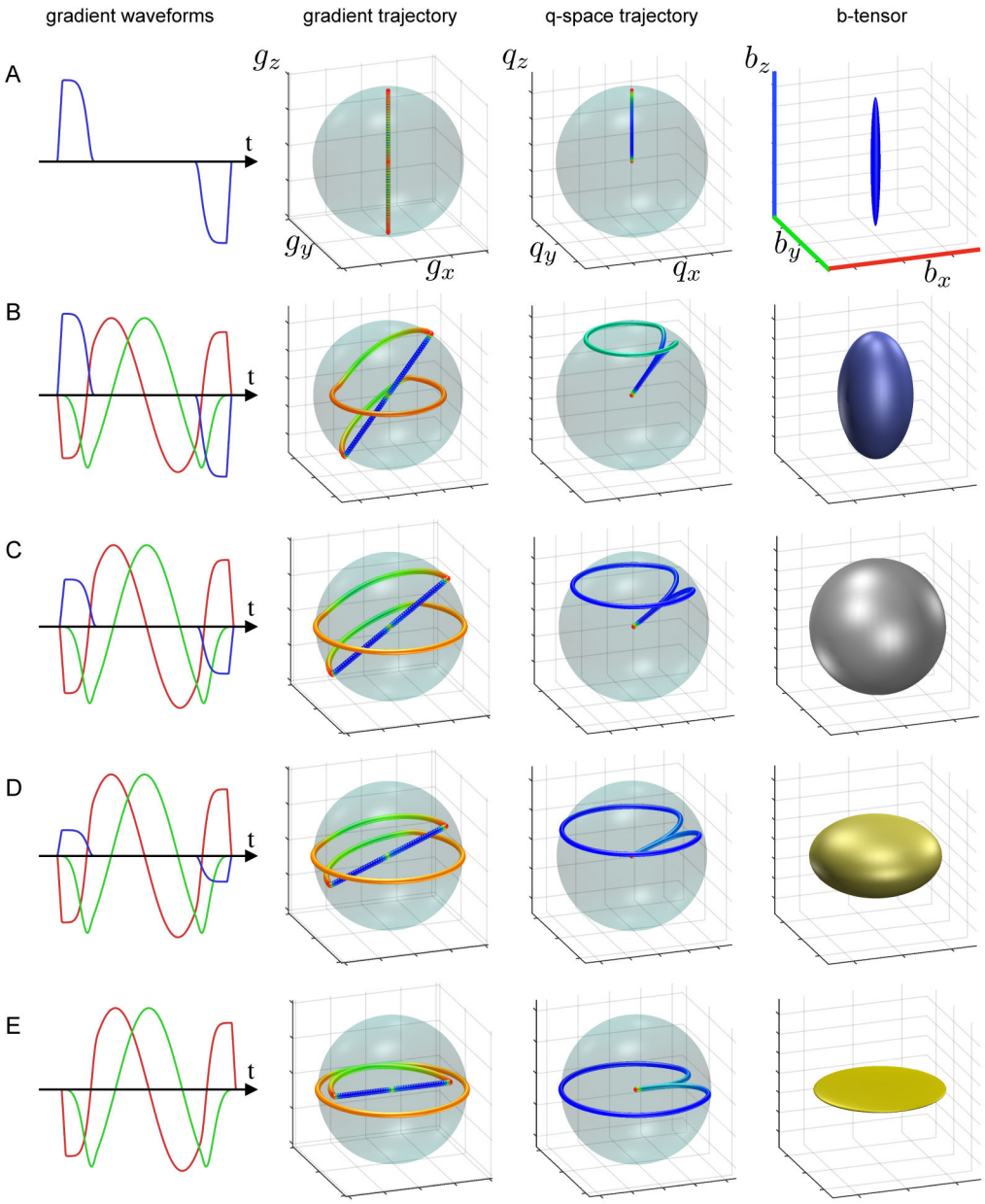

Fig. 4.

QTE encoding: an example family of b-tensors, with shapes ranging from linear to spherical to planar. Gradient waveforms and trajectories are shown along with the resulting q-space trajectories and b-tensors. The curves were produced by transforming the curve with efficient isotropic encoding (C) to yield linear encoding (A), prolate encoding (B), oblate encoding (D), and planar encoding (E). We have used b-tensors from this family in our proof-of-concept clinical study, where multiple rotated versions of this family were applied.

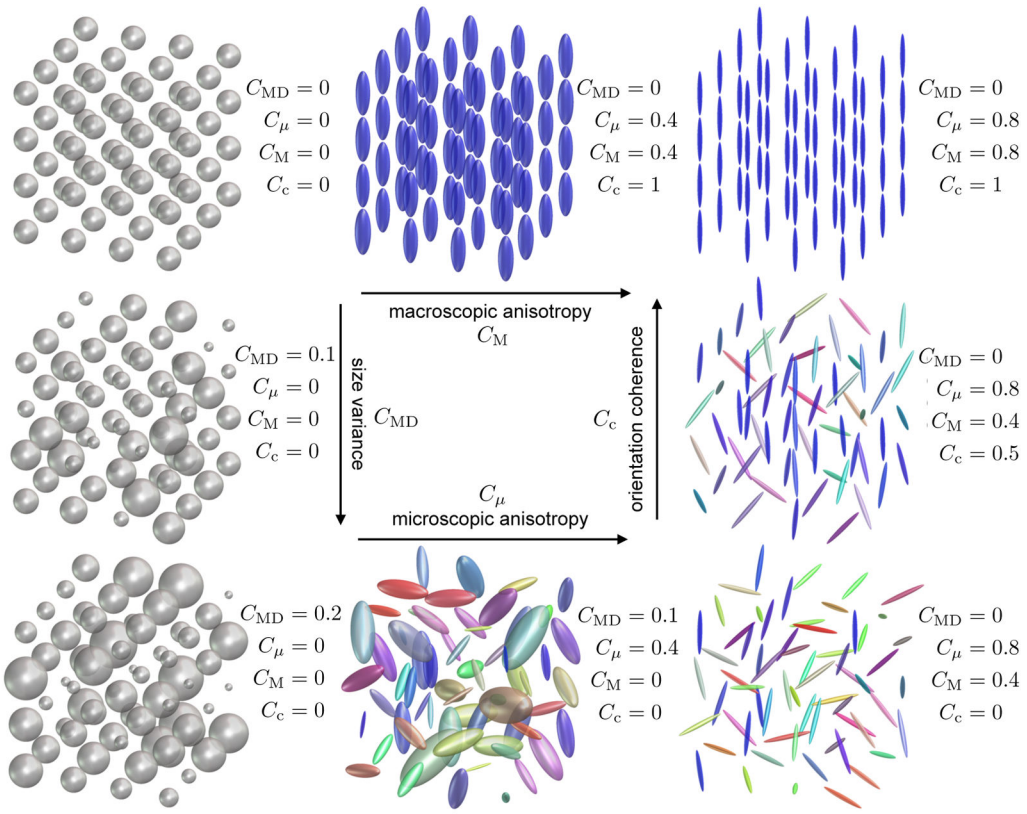

Fig. 5.

This visualization of four proposed measures demonstrates how the measures would change in eight illustrative synthetic macrodomains (voxels). Note that these measures intuitively separate size, shape, and orientation coherence, as well as providing the traditional macroscopic anisotropy.

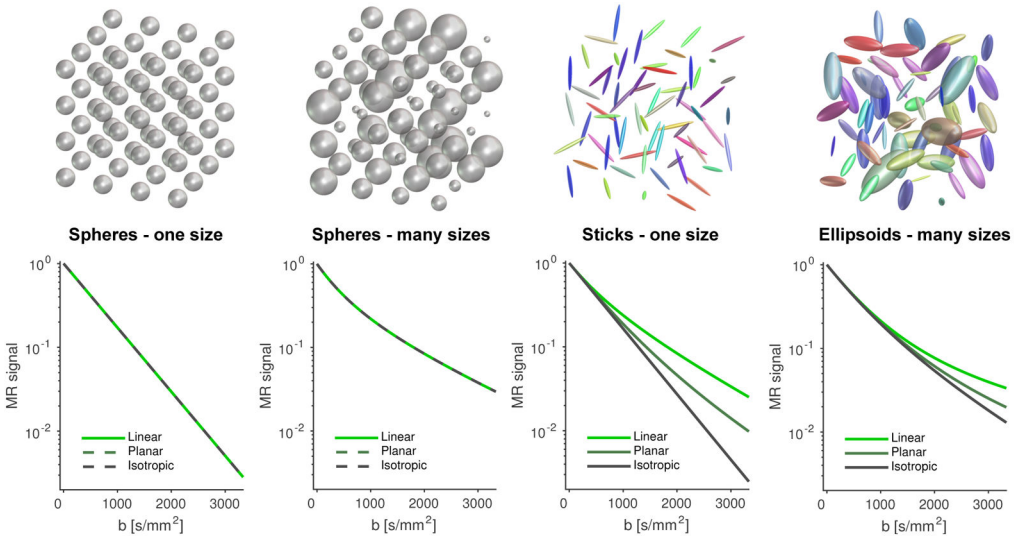

Fig. 6.

The signal plots show the MR signal versus b-value measured in four synthetic datasets using b-tensors of three different ranks, where ranks are identified with shapes such that rank 1 is “linear,” rank 2 is “planar,” and rank 3 is “spherical.” The four synthetic datasets represent four distinct scenarios with different distributions of microenvironments (spheres of one size, spheres of many sizes, sticks of one size and multiple orientations, and ellipsoids of multiple sizes and orientations). Notice the similarities of the light green signal curves in the second, third and fourth plots. This illustrates that when using traditional SDE (linear b-tensor), multiple different microenvironments can produce similar signal responses. In fact, they may even be identical. This shows that using simple model-based estimation of the distribution using SDE data and a predefined model of specific shape, a distribution over size and orientation of that shape that fits the data can always be found, but the parameters found will of course be meaningless if the predefined model does not reflect the underlying tissue architecture.

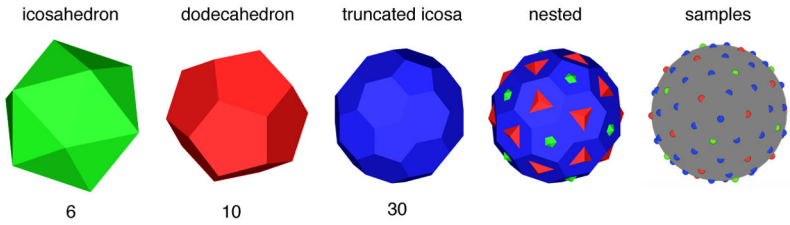

Fig. 7.

In the proposed sampling scheme, Platonic solids are used to ensure even sampling in all directions [55]. Number of distinct sample directions are listed below each solid. Note the dual nature of the icosahedron and dodecahedron: the center of the each face of the icosahedron corresponds to the vertex of the dodecahedron, and vice versa. Further, the center of each face of the truncated icosahedron corresponds to a corner in either the icosahedron or dodecahedron. When the icosahedron, dodecahedron, and truncated icosahedron nest, their vertices (right) give evenly spaced sampling directions. To employ this scheme, a gradient waveform is rotated so that the symmetry axis of its b-tensor aligns with the desired direction (Table 2).

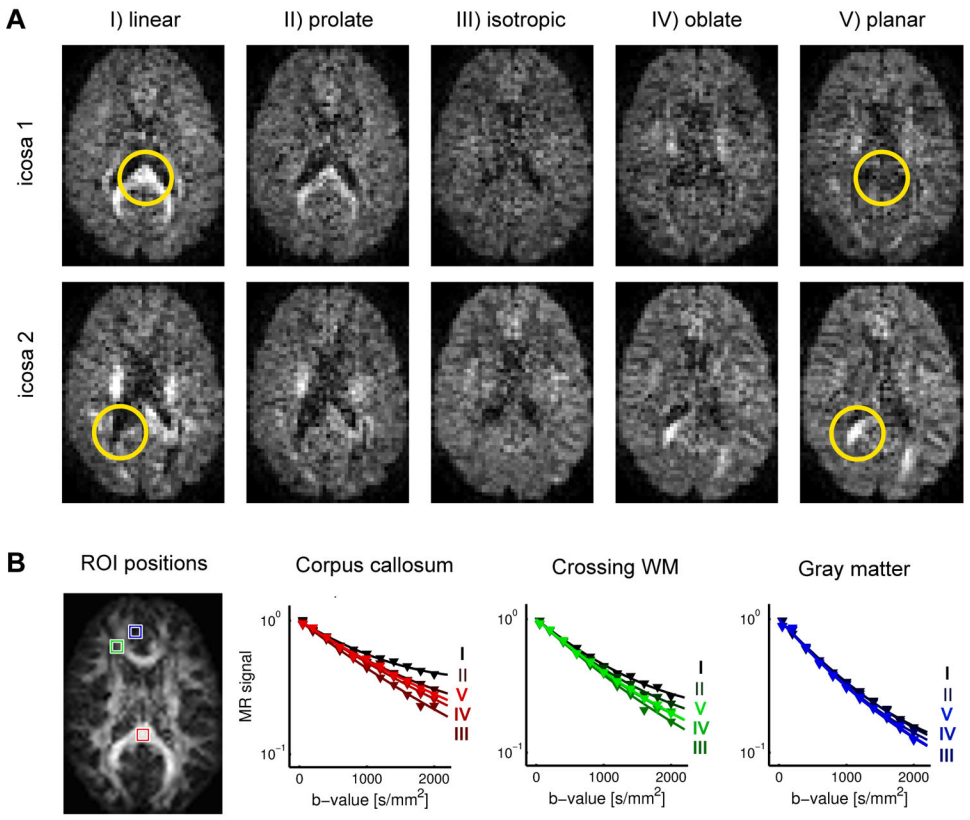

Fig. 8.

In vivo data from the preliminary data set. A. MR images diffusion encoded with $b = 2000$ s/mm^2 and b-tensors of five shapes, i.e., linear, prolate, isotropic, oblate, and planar. Data is displayed from two different b-tensor rotations (directions) sampled from the icosaheadron (icosa 1 and icosa 2, top and bottom rows). Note that the linear and the planar measurements are dual, and thus, where the linear measurement is bright the planar is dark; see yellow circles. This can be compared to the Funk-Radon transform that is performed in q-ball imaging, where the diffusion signal is the result of integration on a great circle [61]. The planar measurement inherently does this integration. B. Signal-versus-b curves averaged across all directions for corpus callosum (red), crossing white matter (green) and gray matter (blue). Curves are encoded with increasing color brightness from linear (dark, I), through prolate (II), isotropic (III), oblate (IV) to planar encoding (full color, V). As expected, the linear encoding attenuates the signal the least, while the isotropic encoding attenuates it the most, and the attenuations from the other encodings are in between. This in vivo data can be compared to the synthetic curves from Figure 6, motivating the need for a model, such as the DTD, that can decipher this data.

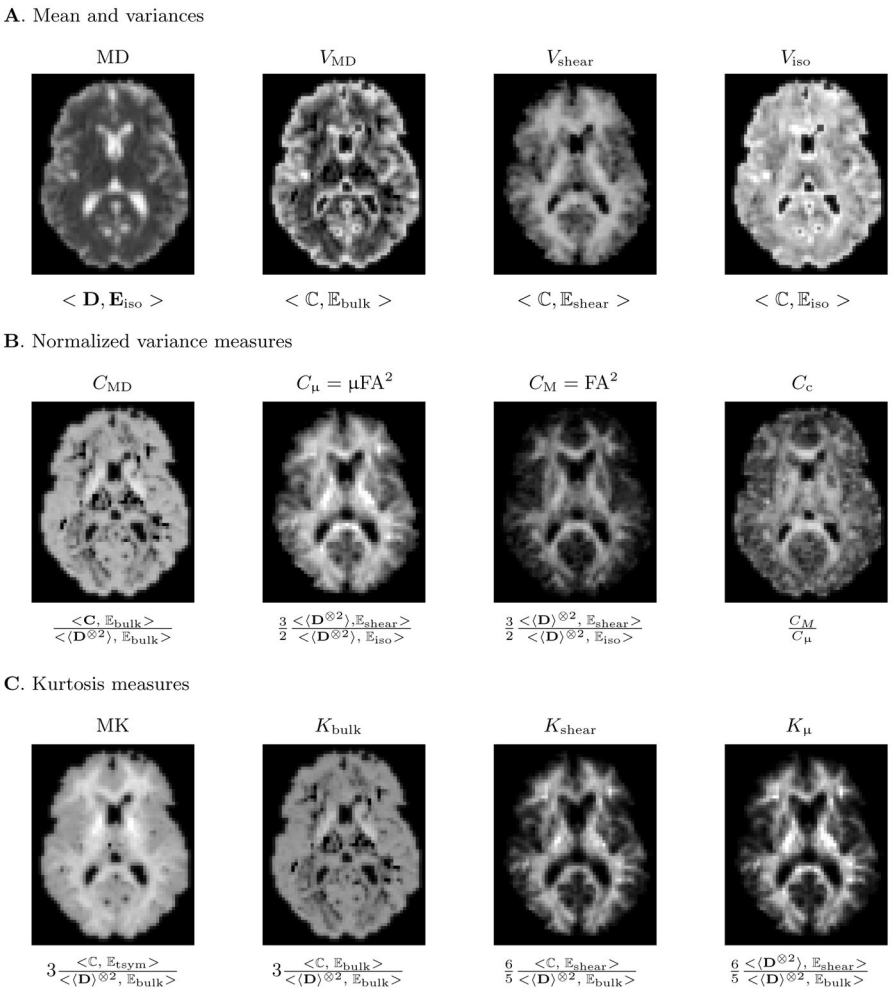

Fig. 9.

Examples of parameter maps obtained in QTI, calculated from data acquired with the clinical protocol. **A**. Top row shows the mean diffusivity MD (Eq. 14), the bulk V_{MD} and shear variances V_{shear} (Eqs. 19, 22), and their sum V_{iso}. **B**. Middle row shows examples of normalized variance measures. **C**. Lower row shows different kurtosis measures derived from QTI: Total mean kurtosis (MK, Eq. 37) separated into two components, bulk and mean kurtosis represented by K_{bulk} and K_{shear}(Eq. 41) and (Eq. 42). The anisotropy-related kurtosis K_{μ} (Eq. 43) is shown in the rightmost panel.

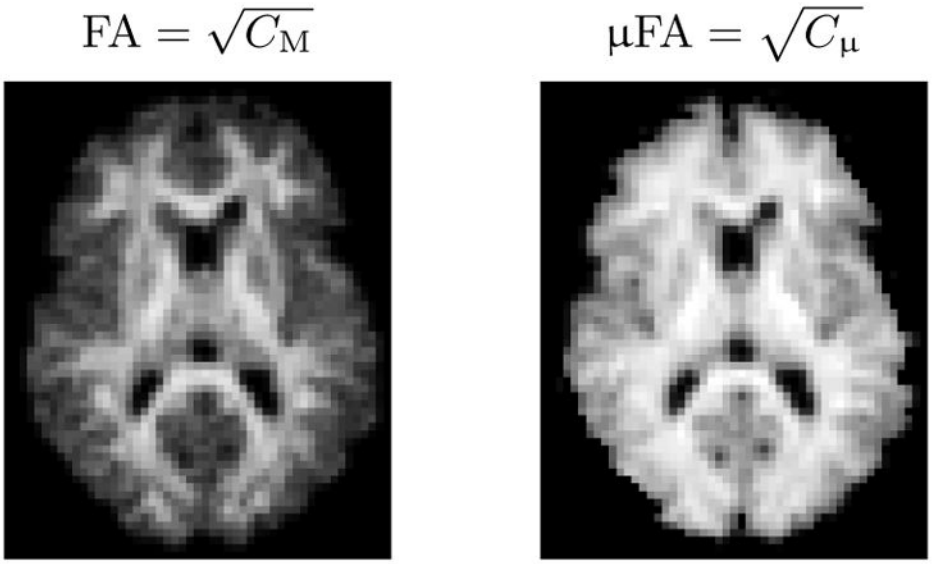

Fig. 10.

The anisotropy measure FA and the microscopic anisotropy μFA, which is known from previous DDE and qMAS studies [9, 51], are straightforwardly calculated from C_M and C_μ.

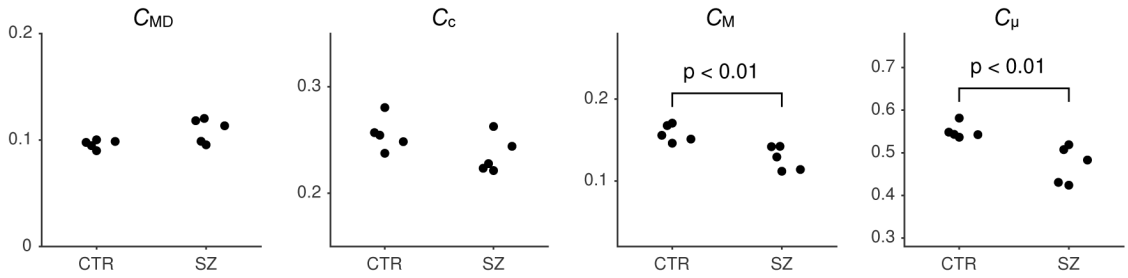

Fig. 11.

Comparison of normalized measures in schizophrenia patients (SZ) and healthy controls (CTR). The C_{MD}, C_M and C_μ averaged across the white matter were all three significantly reduced in the schizophrenia group. Changes in C_c was not found to be significant between the groups. Significance was tested using the Wilcoxon rank-sum U-test.

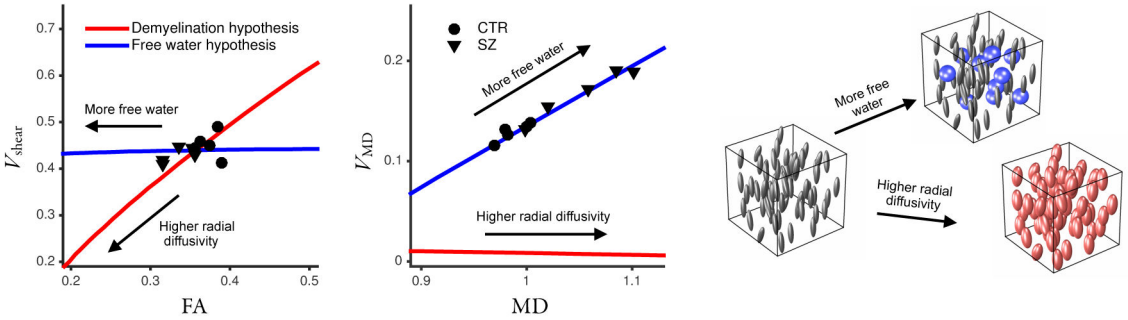

Fig. 12.

Comparison of measured data to simulations of two hypothesized pathologies in schizophrenia. Scatter plots show V_{shear} versus FA (left) and V_{MD} versus MD. Data points represent an average across the cerebral white matter. The two parameters V_{MD} and V_{shear} are related to variances of the distribution, corresponding to changes in size, and changes in orientation/shape respectively. FA and V_{shear} were weakly correlated. MD and V_{MD} were strongly correlated. Solid lines show results from analysis of data simulated to represent a demyelination hypothesis, i.e. increasing radial diffusivity (red), and a free-water hypothesis, i.e. replacing WM with isotropic freely diffusing water (blue). Example voxels representing these hypotheses is shown to the right.

Table 1

Relationship between diffusion imaging method, diffusion encoding technique, q-space sampling strategy, and data modeling methods for current diffusion imaging paradigms and QTI. Example measures include fractional anisotropy (FA), microscopic FA (μFA), and microscopic anisotropy (C_μ).

Method	Diffusion encoding	q-space sampling	Example model/Example measure
DTI	SDE	single shell	diffusion tensor/FA
HARDI	SDE	single- or multi-shell	orientation distribution functions
DSI	SDE	Cartesian sampling	3-D diffusion propagator
DKI	SDE	multi-shell	kurtosis
–	DDE	typically single-shell	μFA
–	TDE	typically single-shell	single-shot diffusion trace
QTI	trajectory encoding	multi-trajectory	DTD/C_μ

Table 2

Overview of the clinical protocol, which includes multiple rotated versions of the family of q-space trajectories in Figure 4. The rotations were defined in order to sample evenly in all directions, using a nested icosahedral sampling scheme (Figure 7). The table includes the number of directions acquired for each b-tensor shape and b-value. The 6 directions were obtained from the icosahedron sampling scheme, 10 from the dodecahedron, 16 from the icosahedron and the dodecahedron, and 30 from the truncated icosahedron scheme [55]. This gives a scheme with in total 216 measurements.

b (s/mm^2)	Stick	Prolate	Sphere	Oblate	Plane
50	–	–	6	–	–
250	6	6	6	–	6
500	10	10	6	–	10
1000	16	16	6	–	16
2000	30	30	6	–	30

Table 3

Comparison of QTI parameters between controls (CTR) and schizophrenia patients (SZ), reported as the group mean (standard deviation). Parameters were averaged across all white matter before the comparison. Significance was tested using the Wilcoxon rank-sum U-test.

Parameter	CTR (n = 5)	SZ (n = 5)	Significance
MD	0.99 (0.01)	1.05 (0.04)	$p < 0.05$
V_{MD}	0.13 (0.01)	0.17 (0.02)	$p < 0.05$
V_{shear}	0.45 (0.03)	0.43 (0.02)	n.s.
V_{iso}	0.59 (0.04)	0.61 (0.02)	n.s.
C_{MD}	0.10 (0.01)	0.11 (0.01)	n.s.
C_{μ}	0.55 (0.02)	0.47 (0.04)	$p < 0.01$
C_{M}	0.16 (0.01)	0.13 (0.01)	$p < 0.01$
C_{c}	0.26 (0.02)	0.24 (0.02)	n.s.
μFA	0.74 (0.01)	0.69 (0.03)	$p < 0.05$
FA	0.37 (0.01)	0.33 (0.02)	$p < 0.01$
MK	0.93 (0.05)	0.90 (0.03)	n.s.
K_{bulk}	0.31 (0.01)	0.36 (0.04)	$p < 0.05$
K_{shear}	0.62 (0.04)	0.53 (0.06)	$p < 0.05$
K_{μ}	0.79 (0.05)	0.67 (0.07)	$p < 0.01$